





3 1293 01716 3472

This is to certify that the
dissertation entitled
"Electron Dynamics in Thin Epitaxial Cu(100) Films
Studied by Adsorbate Induced Broadband Reflectance
and Resistivity Change Measurements"
presented by

EVSTATIN TODOROV KRASIEV

has been accepted towards fulfillment
of the requirements for

Ph.D. degree in Physics


Major professor

Date November 14, 1997

LIBRARY
Michigan State
University

PLACE IN RETURN BOX
to remove this checkout from your record.
TO AVOID FINES return on or before date due.

DATE DUE	DATE DUE	DATE DUE

**ELECTRON DYNAMICS IN THIN EPITAXIAL Cu(100) FILMS STUDIED BY
ADSORBATE INDUCED BROADBAND REFLECTANCE AND RESISTIVITY
CHANGE MEASUREMENTS**

By

Evstatin Todorov Krastev

A DISSERTATION

**Submitted to
Michigan State University
in partial fulfillment of the requirements
for the degree of**

DOCTOR OF PHILOSOPHY

**Department of Physics and Astronomy
Center for Sensor Materials**

1997

ABSTRACT

ELECTRON DYNAMICS IN THIN EPITAXIAL Cu(100) FILMS STUDIED BY ADSORBATE INDUCED BROADBAND REFLECTANCE AND RESISTIVITY CHANGE MEASUREMENTS

By

Evstatiin Todorov Krastev

Gas adsorption on clean metal surfaces has been actively investigated in recent years. It was found that for a number of systems the adsorbed gas causes a decrease in the broadband infrared reflectance of the metal surface. The fractional reflectance change $\Delta R/R$ is too big and of the wrong sign to be accounted for by the dielectric properties of the adsorbates. This effect has been explained by an increase in the diffuse conduction electron scattering from the surface due to the adsorbates. The model also relates $\Delta R/R$ to an increase in the resistivity $\Delta\rho$ of the metal.

I present an experimental test of the linear relationship between $\Delta R/R$ and $\Delta\rho$ predicted by the scattering model. The samples used were epitaxial Cu(100) thin films thermally evaporated on Si(100) substrates. A great deal of effort was put into developing the deposition techniques and characterizing the crystal structure, surface quality and electrical properties of the films. The epitaxy was verified by X-ray crystallography and low energy electron diffraction. The films exhibit 3-D growth with an rms surface roughness of 1 to 2 nm on a $1\ \mu\text{m}^2$ scale, found by atomic force microscopy in air. Films

of thickness 50 nm exhibit 2 to 3 times higher resistivity than pure bulk Cu. Auger electron spectroscopy detected carbon and oxygen levels of less than 5 atomic percent, with no other impurities above ~2%.

Simultaneous *in situ* measurements of changes in the dc resistivity and broadband infrared reflectance induced by oxygen and formate (HCOO) adsorption on the Cu films demonstrate that the mechanism of the resistance change is chemically specific. For oxygen, a linear relationship between the resistivity and reflectance changes confirms that conduction electron scattering is dominant, as previously deduced from infrared measurements on single crystals. The experimental values of the proportionality constant show a wide spread and in most cases deviate from the theoretical value based on the electron density in bulk copper.

On identically prepared Cu films, adsorbed formate induces a comparable resistivity change, but *no* detectable reflectance change. This difference is inconsistent with the scattering mechanism, for which the ratio of the two effects should depend only on the substrate and not on the adsorbate. The resistivity change induced by formate may arise from a reduction of the conduction electron density.

This work is the first study based on *in situ* measurements of well characterized samples demonstrating *striking deviation from the scattering model*. It is a strong motivation for further experimental and theoretical work in order to clarify the mechanisms through which adsorbates affect the electron dynamics of metal thin films.

To My Family

ACKNOWLEDGMENTS

First I want to thank Prof. Roger Tobin, who guided me through the long process of working towards completion of this dissertation. He taught me so many things for which I am deeply grateful. He helped me through times difficult for me, not just being my advisor but a good friend.

I want to thank my beautiful wife Karen for her love, encouragement, and the joy and happiness she brought into my life.

I am grateful to my mother Ivanka, father Todor and sister Vessela. Although they are far away in Bulgaria, I have always felt their love, support and concern about me.

Many people in the Department of Physics and Astronomy at MSU have contributed to this work by providing valuable help and assistance. I enjoyed working with Tom Palazzolo, Jim Muns and Tom Hudson at the machine shop. Their expertise and advice has always been of great benefit to my design work. I strongly appreciate the assistance from Stephanie Holland, Ann Kirchmeier, Sandy Teague and Mary Curtis. They made my life much easier. I am thankful to Prof. Jerry Cowen for providing me with an office during the last year and being always very nice. My coworkers, which I shared my time in the lab with, deserve special regard -- Dennis Kuhl, Ching-Ling Hsu, Larry

Voice, Kathy Lin and Hong Wang. I learned a lot through our common work and being with them was always fun.

I thank the Center for Electron Optics of the Pesticide Research Center, Michigan State University, for the use of its AFM facility and Stanley Flegler for his help and valuable advise. I thank Thomas R. Bieler and Cheong Soon-Wuk, Department of Material Science and Mechanics, Michigan State University for their help in obtaining and analyzing pole figures of our thin films.

I am grateful to the people at the Center for Sensor Materials at MSU, as most of my funding came from there. This work was supported by the National Science Foundation under Grant Nos. DMR-9201077, DMR-9510267, DMR-9696233 and DMR-9400417 (MRSEC).

Last, but not least I want to thank Branislav (Bane) Blagojevic, Gyorgy Filep and all the numerous friends of mine for the nice times spent together and the exciting memories, which I will carry with me wherever I go.

TABLE OF CONTENTS

List of Tables	ix
List of Figures	x
Chapter 1 Introduction	1
1-1. Motivation for the Study	1
1-2. Electrical Resistivity of Clean and Gas Covered Thin Metal Films	6
1-3. Broadband Infrared Reflectance Change of Metal Surfaces Due to Gas Adsorption	14
1-4. Relation Between the Adsorbate-Induced Broadband IR Reflectance and DC Resistivity Change of Thin Metal Films	24
References	32
Chapter 2. Apparatus and Experimental Technique	35
2-1. Far-infrared surface spectroscopy system	35
2-1-1. Optical setup	37
2-1-2. Main UHV chamber	40
2-2. Thin film sample preparation	42
2-3. Combined Resistivity and Broadband Reflection Change Measurement of Thin Cu(100) Films Due to Gas Adsorption	46
2-3-1. Resistivity Change Measurement	46
2-3-2. Broadband Reflectance Change Measurement	49
References	52

Chapter 3. Development of a Novel UHV Sample-Transfer and Sample-Handling System	54
3-1. Introduction	54
3-2. General Operation of Our UHV Transfer System	57
3-3. Carrier Disk	62
3-4. UHV Sample Mount	64
3-5. Concluding Remarks	67
References	69
Chapter 4. Surface Morphology and Electrical Conductivity of Epitaxial Cu(100) Films Grown on H-Terminated Si(100)	71
4-1. Introduction	71
4-2. Film structure and surface morphology	73
4-3. Electrical conductivity	84
4-4. Conclusions	90
References	92
Chapter 5. Multiple mechanisms for adsorbate-induced resistivity: Oxygen and formate on Cu(100)	94
5-1. Introduction	94
5-2. Experimental	97
5-3. Results and Discussion	99
References	107
Chapter 6. Conclusion	110
References	115

LIST OF TABLES

Table 1-1. Adsorbate induced fractional reflectance change $\Delta R/R$ for adsorbate coverage n_a measured experimentally and calculated using equation 1-28 and published values for $t\Delta\rho$. The table is reproduced from reference [40].	29
Table 1-2. Comparison of the theoretical and experimental values for the slope of the linear dependence between reflectance change and DC resistivity change for different adsorbates on Cu and Ag polycrystalline films. The table is reproduced from the study by Hein and Schumacher [45].	30
Table 4-1. Characteristics of 100 nm copper films annealed in vacuum at different temperatures. All of the films were deposited at rates of 0.1 - 0.2 nm/s, with no intentional heating of the substrate during deposition.	82
Table 5-1. Values of the coefficient ne^2/mc deduced from the slope of $\Delta R/R$ vs. $t\Delta\rho$.	102

LIST OF FIGURES

- Figure 1-1.** Conductimetric sensing. a) clean surface, b) adsorbates on the surface - the resistance increases, c) combined broadband reflectance and resistivity change measurement. 4
- Figure 1-2.** Resistivity increase due to gas adsorption on thin metal films for different gas-substrate systems. The figure is reproduced from reference [17]. 12
- Figure 1-3.** Broad-band reflectance change for 0.25 ML oxygen adsorption on Cu(100) single crystal for the frequency range 200 - 2000 cm^{-1} . The gaps in the spectrum and the noise at high frequencies are due to the poor transmittance of the polyethylene windows. The solid line is a fit to the Persson-Volokitin scattering model. The graph is reproduced from reference [41]. 15
- Figure 1-4.** Antiabsorption resonance observed by Hirschmugl *et al.* [37] using RAIRS. The absorption of the IR light decreases at the resonance frequency. The graph is reproduced from reference [28]. 17
- Figure 1-5.** Specular and nonspecular scattering of conducting electrons at the surface. 19
- Figure 2-1.** Layout of the far infrared surface spectroscopy system. Reproduced from reference [1] by C. Chung. 36
- Figure 2-2.** Comparison between AES scans for Cu films grown on not annealed (a) and annealed at 750K (b) Si substrate. The surface of the not annealed film is contaminated with about 23 atomic percent (a.p.) C and 3 a.p. O. The surface of the film grown on annealed Si substrate is much cleaner with C and O peaks comparable to the noise level. 44

- Figure 2-3.** Resistivity change of Cu(100) film due to 50L formic acid exposure - a) row data - voltage drop across the sample, registered by the LIA, b) the linear baseline is removed and the fractional resistivity change $\Delta\rho/\rho$ calculated. The maximum $\Delta\rho/\rho$ is about 1.1%. 48
- Figure 2-4.** Broadband reflectance change $\Delta R/R$ of 50 nm thick Cu(100) film exposed to 50 Langmuirs (5×10^{-7} Torr for 100 seconds) of oxygen. The measurement is performed at room temperature. Total $\Delta R/R$ is about 0.5%. 50
- Figure 3-1.** Main components of the UHV sample transfer system. 58
- Figure 3-2.** Starting at 105 K a copper sample is heated up to 740 K, driving the sample heater at 9.8 Amp. After that the sample heater is turned off and the sample is cooled down to 115K. 60
- Figure 3-3.** Sample carrier disk. 61
- Figure 3-4.** UHV sample mount. 65
- Figure 4-1.** θ -2 θ X-ray diffraction pattern of 100 nm thick Cu film deposited on H-terminated Si(100) at 0.1-0.2 nm/s evaporation rate, without intentional heating. The strong Cu(200) peak and absence of a Cu(111) peak indicate highly oriented growth. 74
- Figure 4-2.** Cu(111) X-ray pole figure of a 100 nm copper film grown on H-terminated Si(100). Equal areas in the figure represent equal solid angles. The four sharp poles at $\Theta = 55^\circ$ demonstrate that the Cu film is epitaxial. The inset shows a scan through one of the poles in the azimuthal (Ψ) direction keeping the radial angle constant ($\Theta=55^\circ$). The width of the pole is instrument-limited. 76
- Figure 4-3.** AFM topographical images of area $1 \times 1 \mu\text{m}^2$ for two different film thicknesses -- a) 7.5 nm and b) 100 nm. The z-range for both images is 10 nm and the RMS roughness is 0.71 nm for (a) and 0.95 nm for (b). Both films were grown near room temperature and were not annealed. 77
- Figure 4-4.** RMS roughness vs. deposition rate for 100 nm thick films grown without intentional heating of the substrate. Each data point represents a $1 \times 1 \mu\text{m}^2$ area of a different sample. 79

- Figure 4-5.** AFM topographic image of area $1 \times 1 \mu\text{m}^2$ of a 100 nm Cu film grown under conditions nominally identical to those for the film shown in Fig. 3b. The z -range is 20 nm, and the RMS roughness is 1.8 nm. Note the much larger grains and deeper holes. 80
- Figure 4-6.** AFM topographical image of a 100 nm Cu film annealed in vacuum at 175°C after deposition near room temperature. The z -range is 61 nm. The channels penetrate deep into the film, nearly to the Si surface. 83
- Figure 4-7.** Apparent resistivity of a Cu film of thickness $t = 120$ nm grown near room temperature at approximately 0.1 nm/s. The dashed line is the best fit to the Fuchs-Sondheimer theory, Eq. 2. The solid line assumes an initial insulating layer of thickness t_0 , Eq. 5. The fitting parameters are given in the text. 85
- Figure 4-8.** Effective conductivity $\sigma_{eff}(t)$ (defined by Eq. 1) of the same Cu film as in Fig. 7. The dashed line is the best fit to the Fuchs-Sondheimer theory, Eq. 4. The solid line assumes an initial insulating layer of thickness t_0 , Eq. 5. The fitting parameters are given in the text. The inset shows the 0 - 30 nm region on an expanded scale. The arrow indicates the conductivity of pure Cu at the deposition temperature. 86
- Figure 5-1.** a) Fractional reflectance change at 2650 cm^{-1} for oxygen on epitaxial Cu(100). The film was 49 nm thick. At 110 s the sample was exposed to 5×10^{-7} Torr O_2 for 100 s. b) Fractional dc resistivity change measured simultaneously with (a). 100
- Figure 5-2.** Fractional reflectance change $\Delta R/R$ vs. $t\Delta\rho$ for oxygen on epitaxial Cu(100), from Fig. 1. The error bar shown is typical of all the points. 101
- Figure 5-3.** a) Fractional reflectance change at 2650 cm^{-1} for formate on epitaxial Cu(100). The film was 51 nm thick. At 130 s the sample was exposed to 5×10^{-7} Torr formic acid for 110 s. No reflectance change is observable. b) Fractional dc resistivity change measured simultaneously with (a). 103

Chapter 1

Introduction

1-1. Motivation for the Study

Surface science is the study of atomic arrangements and chemical complexes on solid surfaces and interfaces, their electronic, mechanical and chemical properties. Due to the interdisciplinary nature of the observed phenomena it is in the spheres of vital interest for both physicists and chemists. From a technological point of view there are many processes which benefit from a better understanding of the processes occurring at surfaces and interfaces. These include the industrial fields of crystal growth, chemical sensing, corrosion, catalysis, semiconductor interfaces to name a few.

There are several landmarks in the development of *surface science* as a separate discipline, which should be noted. The first one is the concept of monolayer adsorption. It was introduced by Langmuir in 1916 [1] and is considered to be of revolutionary importance [2]. Most of the earlier studies had been concerned with adsorption on porous materials with the adsorbed layers being thought to be thousands of molecular diameters thick due to highly underestimating the area of the surface. Langmuir studied the chemisorption of different gases on a tungsten filament which is completed at one monolayer coverage. His understanding of the chemical bonding, arising from

nonsaturated or dangling bonds at the surface and the localization of the adsorbed species at certain locations (sites) are among the basics in the contemporary theory.

The second landmark is considered to be the work by Lennard-Jones in 1932 [3]. All the earlier theoretical developments had been semi-empirical with very little involvement of quantum mechanical concepts. The experimental studies had been mostly occupied with thermodynamical quantities - determination of isotherms and adsorption heats using calorimetry. Lennard-Jones developed a quantum mechanical representation of the potential energy of an adatom at the surface and clarified the distinction between physisorption in terms of van der Waals' forces and chemisorption due to chemical bonding.

The third, rather technical than scientific development of crucial importance for contemporary surface science was the progress of technology in obtaining a commercially available clean environment for conveying the surface experiments - a good enough vacuum and the means of measuring it. In the 1930s attaining pressures of 10^{-6} Torr was routine using rotary oil and mercury-diffusion pumps and elastomer seals. At that pressure, each second about 5×10^{14} molecules from the ambient residual atmosphere arrive on each square centimeter of the surface. Considering that an atomic monolayer corresponds to about 10^{15} atoms per cm^2 , a monolayer of "junk" forms in a couple of seconds on the "clean" surface of the studied material, which makes it impossible to carry out surface experiments. Nowadays pressures in the range of 10^{-10} Torr and lower are considered adequate for the needs of the surface scientist. This is the so called ultrahigh vacuum (UHV), which became possible by development of metal seals, new types of

pumps (ion, titanium sublimation and sorption) and gauges (Bayard-Alpert, quadrupole and crossed field spectrometer). At UHV pressure about a monolayer of molecules on the surface is formed in about 8 hours giving “enough” time to perform an experiment. By my experience the time is never enough due to the very delicate nature of the surface work and obtaining a “good” experiment often takes many attempts and long hours.

The last 30 years mark a period of large development in the field of surface science. Sufficiently good theories for the band structure and chemical bonding of bulk solids became available. This inspired extension of the theories and their experimental examination to the more complicated case of surfaces. Progress in computing capabilities facilitated the development of theoretical models and the commercial availability of UHV provided the test environment. The last but not the least factor was the strong *technological* need for better fundamental understanding of the physical and chemical processes occurring at surfaces and interfaces.

Due to the immense significance of thin metal films in such areas as chemical sensing and microelectronic devices, the understanding of their structural and electronic properties is extremely important from a technological point of view. My work is a study of the crystal structure, surface morphology and electronic transport properties of thin copper films on silicon substrates using the tools of the surface scientist. The simple concept of "conductimetric sensing" - the increase of the resistivity of different materials upon gas adsorption on the surface - is the basis for wide variety of commercial gas sensors (Figure 1-1a,b). It is well known that the adsorbed gas molecules also affect the reflectance of metals. In an attempt to better understand the fundamental mechanisms

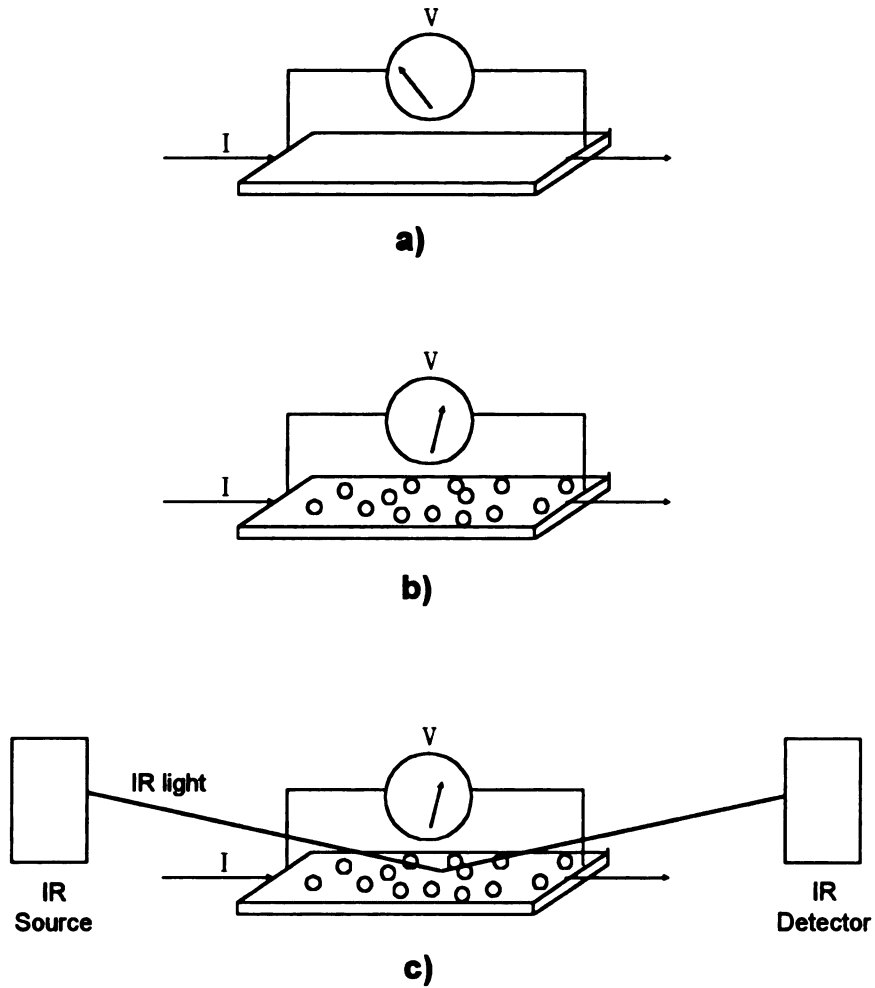


Figure 1-1. Conductimetric sensing. a) clean surface, b) adsorbates on the surface - the resistance changes, c) combined broadband reflectance and resistivity change measurement.

underlying these effects, my work was concentrated on performing *in situ* broadband infrared (IR) reflectance measurements together with resistivity measurements of well characterized samples (Figure 1-1c). The ultimate goal was to check the validity of the earlier proposed mechanism [4-7], which attributes the resistivity and reflectance changes observed experimentally to diffuse scattering of the conduction electrons in the film by the potential of the adsorbates, randomly distributed on the surface. Later in this chapter I will discuss the scattering theory in detail.

To perform the above experiments there was a need for a suitable substrate, which had to conform to variety of requirements. The material needed to be a well characterized metal, thin enough for the change in the resistivity to be easily detected, and thick enough to act as bulk for the infrared light. Our choice fell on copper films of thickness 50 to 100 nm because they meet the above requirements (the skin depth δ for bulk copper is 27 nm [8]) and there was evidence in the literature [9-17] that it is not difficult to grow well ordered thin Cu films on H-terminated Si(100) and Si(111). The plan of my work was as follows. First, develop the techniques for growing epitaxial Cu(100) films on Si(100) substrates in a high vacuum evaporator and characterize their crystal order, surface quality and electrical properties. Second, design and build an ultrahigh vacuum (UHV) transfer and evaporation system for the UHV chamber that is part of our infrared spectroscopy system. We considered designing our own transfer system because there was no commercial one suitable for our requirements -- move large samples 1 1/4" x 1/2" through relatively small ports (1 3/8" diameter), available on our UHV chamber, position precisely inside the chamber and make 6 electrical contacts with the sample holder. All of the above

also needed to be at a reasonable price. Once the equipment was tested and functional I had to perform *in situ* combined broadband reflectance and resistivity change measurements of our thin copper films using oxygen and formate as adsorbates, analyze the data, and look at the results from the point of view of the existing theory.

1-2. Electrical Resistivity of Clean and Gas Covered Thin Metal Films

Because of their large technological importance, thin metal films have been an object of a lot of experimental and theoretical work [18-20] in recent years, aimed at better understanding their electrical and structural characteristics. Experimentally there is a significant inconsistency in the data published by different authors. The reason is that the films differ considerably in their properties because of variation in the deposition conditions. Therefore for a reliable study it is very important that the films are grown in an UHV environment and that their structural and electrical properties are well characterized.

Usually experiments show that the resistivity of clean thin films is higher (up to 10 times) than the resistivity of a bulk single crystal material. Most of the theories explain this effect with a decrease in the mean free path of the electrons due to surface scattering or bulk scattering of point defects, dislocations, grain boundaries and impurities.

A size effect treatment by Fuchs [21] and Sondheimer [22] assumes that a fraction of the conducting electrons scatter diffusely at the surfaces of the film this way increasing the resistivity. The parameter p , called the Fuchs specularity parameter, is the fraction of the conducting electrons specularly reflected by the film surfaces. The experimental data

for this parameter show extremely high variations which are not explained well in the literature so far. The above theory makes several simplifying assumptions, some of them not well realized in real films:

- 1.) the film possesses ideal plane parallel interfaces.
- 2.) the disorder is considered independent of the film thickness
- 3.) single parabolic conduction band
- 4.) the scattering is isotropic, characterized by scattering parameter p and single mean free path l .

The result from solving the Boltzmann transport equation for the resistivity ρ of the film under assumptions 1-4 is [18]:

$$\frac{\rho_o}{\rho} = 1 - \frac{3}{2}x(1-p) \int_x^{\infty} \left(\frac{1}{s^3} - \frac{x^2}{s^5} \right) \frac{1-e^{-s}}{1-pe^{-s}} ds, \quad (1-1)$$

where ρ_o is the resistivity of the bulk with the same concentration of lattice defects as the film, $x = t/l_o$, t is the film thickness and l_o is the bulk mean free path.

For $t \gg l_o$ (1-1) simplifies to:

$$\rho = \rho_o \left[1 + \frac{3}{8}(1-p) \frac{l_o}{t} \right]. \quad (1-2)$$

For $x > 0.2$, which usually applies for thin films, equations (1-1) and (1-2) agree to better than 10 %.

A theory by Mayadas and Shatzkes employs a one dimensional grain boundary model, with crystallite size D , eliminating assumption 2. The idea is similar to the Fuchs-Sondheimer, but employing different limits for integration of the Boltzmann equation. The result for resistivity is [18]:

$$\rho = \rho_o \left[1 + \frac{3}{2} \frac{R}{1-R} \frac{l_o}{D} \right], \quad (1-3)$$

where R is the part of the conducting electrons specularly reflected at grain boundaries, ρ_o and l_o have the same meaning as in equation 1-2.

The scattering hypothesis [18] uses the concept of extra resistivity induced by lattice disorder and diffuse surface scattering and the resistivity is given by:

$$\rho = \rho_o \left[1 + Z^* A^* \frac{l_o}{D} + ZA \frac{l_o}{t} \right]. \quad (1-4)$$

Here Z and Z^* are the number of scattering centers per cm^2 of the film surface and inner crystallite surface respectively, A and A^* are the mean scattering cross section at the film surfaces and grain boundaries respectively and ρ_o is the resistivity of defectless film.

Equation (1-4) is pretty much a combination of equations (1-2) and (1-3) via the Mathiessen's Rule.

Calculations in reference [18] show that all of the above theories give similar results for the thickness dependence of the film resistivity. This is feasible, as all of them assume that diffuse scattering of conducting electrons is the main reason for higher than the bulk film resistivity, usually found by the experiment. The concept of diffuse electron scattering was first introduced by Fuchs and Sondheimer.

An approach, which takes into account film roughness is introduced by Vancea and Hoffmann [23,24]. They start with the expression for the film conductivity $\sigma(t)$ (t is the film thickness) from the Fuchs theory (ideal film with flat parallel surfaces):

$$\frac{\sigma(t)}{\sigma_{\infty}} = 1 - \frac{3}{2}(1-p) \int_1^{\infty} \left[\frac{(s^{-3} - s^{-5})}{1 - p \exp\left(-\frac{t}{l_{\infty}} s\right)} \right] ds. \quad (1-5)$$

The surface roughness exhibited by real films is included in the model by a concept introduced by Namba [25] :

$$\langle \sigma(\langle t \rangle) \rangle = \sigma_{\infty} \frac{L}{\langle t \rangle} \left[\int_0^L t(x) \frac{\sigma_{\infty}}{\sigma(t(x))} dx \right]. \quad (1-6)$$

Here $\langle \sigma(\langle t \rangle) \rangle$ is the *measured* average conductivity, $\langle t \rangle$ is the average film thickness, $t(x)$ is the local film thickness which varies across the film, L is the length of the film, σ_{∞} is

the final film conductivity, and $\sigma(t(x))$ is the local conductivity given by equation 1-5. $t(x)$ is approximated by a one dimensional sinusoidal fluctuation:

$$t(x) = \langle t \rangle + h \sin(2\pi \frac{x}{s}), \quad (1-7)$$

where h is the surface roughness amplitude.

The main characteristic of the Namba model is that $\sigma \rightarrow 0$ for $t = h$, because the film becomes discontinuous. Since many real films are discontinuous at small but non zero $\langle t \rangle$ the model gives a smooth interpolation between the conductivity cutoff and the Fuchs - Sondheimer behavior at larger thickness. Using the Drude conductivity relation for spherical Fermi surfaces, n_α is expressed as:

$$n_\alpha = \left(\frac{3}{8\pi}\right)^{1/2} \left(\frac{h_p}{e^2}\right)^{3/2} \left(\frac{\sigma_\infty}{l_\alpha}\right)^{3/2}, \quad (1-8)$$

where n_α is the conducting electron density in the film and h_p is Planck's constant.

Equations 1-5, 1-6 and 1-7 were computer fitted to the experimentally measured $\langle \sigma(\langle t \rangle) \rangle$ curves for copper, aluminum, silver, gold, nickel and platinum polycrystalline films, evaporated at UHV and high vacuum conditions on glass substrates. The authors emphasize that the Fuchs-Namba model is the only one which could be fitted to their experimental data. From the computer fit the parameters σ_α , h , l_α - mean free path, and p

- the specular parameter were extracted. However it is very difficult and model dependent to separate l_α and p .

A result of the above treatment is that the decreased conductivity σ_α of the thin films (even for a very thick film $\sigma_\alpha < \sigma_{bulk}$), was correlated to a reduction in the conducting electron density n_α , rather than due to decreased mean free path l_α . The determined free electron density for different films varies between 7% and 90% of the expected bulk values. This was explained by quantum mechanical trapping of the conducting electrons inside the separate grains, with the grain boundaries serving as potential barriers, at which the localized electrons scatter elastically. Only the electrons which can tunnel through all the barriers contribute to the conductivity.

So far I have discussed metal films with surfaces as clean as possible. The change of the electronic properties of thin metal films due to gas adsorption is a very important effect technologically because of its application in gas sensing. The experiment usually finds that the film resistivity increases when gas molecules stick on the surface. Figure 1-2 presents resistivity measurements for different gas - substrate systems found in the literature [18].

Typically the resistivity change is linear with coverage during the first stages of adsorption. At higher exposures the curve deviates from linearity, reaching saturation or going through a maximum. It is very important that the surface is not contaminated beforehand. If the latter is the case, a smaller total resistivity increase, dips in the resistivity curve or complete absence of resistivity change could be observed. There are

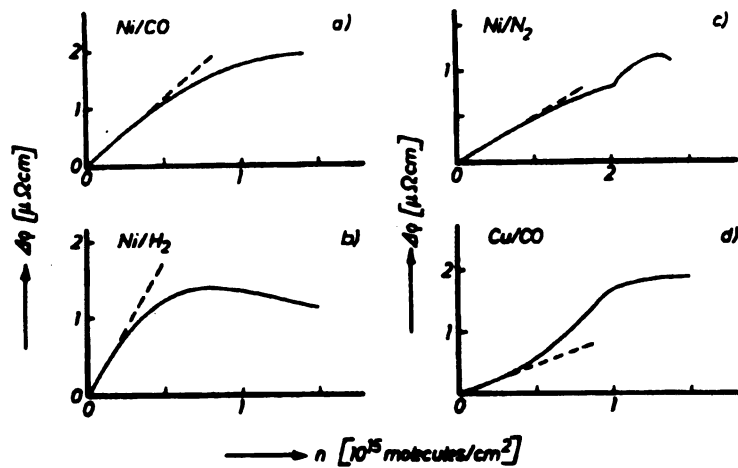


Figure 1-2. Resistivity increase due to gas adsorption on thin metal films for different gas-substrate systems. The figure is reproduced from reference [18].

several competing models attempting to explain the resistivity changes due to gas adsorption, which I will discuss next.

The Suhrmann model [26] attributes the change in resistivity to a direct charge transfer to (or from) the adsorbed molecules, which changes the density of conduction electrons in the near-surface region of the metal. The electron mean free path and the film thickness are assumed not to be affected and the starting point for the model is the Drude free electron gas approximation. The fractional resistivity change $\Delta\rho/\rho$ predicted is:

$$\frac{\Delta\rho}{\rho} = K_1 \frac{n_a}{t}, \quad (1-9)$$

where K_1 is a proportionality coefficient, n_a is the concentration of adsorbed molecules on the surface and t is the film thickness.

Sachtler and coworkers proposed that the binding of conduction electrons by the adsorbate is strong enough to produce an insulating layer at the surface, this way reducing the effective thickness of the metal film [27]. The electron mean free path and the conducting electron density are assumed unchanged. The result is :

$$\frac{\Delta\rho}{\rho} = K_2 h(t, AT) \frac{n_a}{t}, \quad (1-10)$$

where K_2 is a proportionality coefficient, n_a and t have the same meaning as before and the function $h(t, AT)$ can be determined by differentiating the experimental dependence of the resistivity on the deposition parameters, film thickness and annealing temperature (AT).

The third and most widely accepted model - the *Fuchs - Sondheimer scattering model* [21,22] - explains the change in resistivity by an increase in the diffuse scattering of conduction electrons due to the localized potential of the adsorbate, this way affecting the mean free path l_o . If the surface is clean the conducting electrons scatter specularly to some extent even for polycrystalline films. The presence of adsorbates on the surface increases the fraction of the diffusely scattered electrons by creating additional scattering centers. The fractional resistivity change predicted by this model is:

$$\frac{\Delta\rho}{\rho} = K_3 l_o \frac{n_a}{t}. \quad (1-11)$$

The above three competing models were compared by Wissmann [18] in a thorough study of resistivity change due to gas adsorption on copper and nickel thin films. Both materials are *fcc* metals having close values for the lattice constant, but considerably different electronic properties. The influence of the film thickness, annealing temperature, measuring temperature and gas coverage were considered. The experimental data showed deviation from the models by Suhrmann and Sachtler, but was very well fitted to the predictions of the scattering model establishing it as the most accepted one nowadays.

1-3. Broadband Infrared Reflectance Change of Metal Surfaces Due to Gas Adsorption

As the investigation of the interaction of gas molecules with clean surfaces is one of the busiest areas of contemporary *surface science*, different techniques which study the vibrational resonances within the adsorbed molecules or between the adsorbed species and the surface were developed under the collective term *Surface Vibrational Spectroscopy*. Infrared absorption spectroscopy (IRAS), electron energy loss spectroscopy (EELS), and surface enhanced Raman spectroscopy (SERS) are experimental tools revealing the vibrating modes, coupling and energy transfer between the adsorbate and electronic states of the surface. The adsorbates however can also affect the optical response of metal surfaces far from the sharp resonance features - the so called *broadband* response. With the development of high quality surface infrared spectroscopy it became possible to measure these broadband reflectance changes. This type of measurement is more demanding experimentally because it requires the absolute stability of the infrared signal to

be 1% or better during the measurement, in order to reliably register the broadband reflectance change, which is frequency dependent and usually does not exceed 1.5%.

Figure 1-3 shows a measurement of the IR broadband reflectance change of a Cu(100) single crystal due to oxygen at room temperature. The experiment was

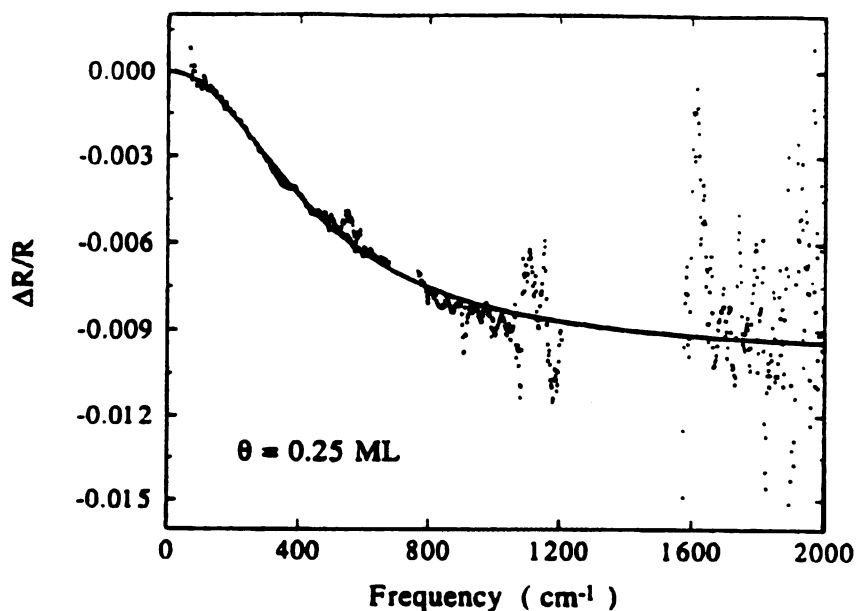


Figure 1-3. Broad-band reflectance change for 0.25 ML oxygen adsorption on Cu(100) single crystal for the frequency range 200 - 2000 cm^{-1} . The gaps in the spectrum and the noise at high frequencies are due to the poor transmittance of the polyethylene windows. The solid line is a fit to the Persson-Volokitin scattering model. The graph is reproduced from reference [28].

performed at the IR synchrotron source at Brookhaven National Laboratory by Lin, Tobin and Dumas[28]. The frequency range between 100 cm^{-1} and 2000 cm^{-1} was covered using two detectors: Si:B bolometer up to 650 cm^{-1} and Ge:Cu photoconductor for frequencies above 400 cm^{-1} . Two sets of measurements were performed - before and after the oxygen

exposure. After averaging, the fractional reflectance change $\Delta R/R$ was calculated and plotted. The gaps in the spectra and the noisier data at higher frequencies are due to the lower transmittance of the polyethylene windows at that frequency range. This measurement is a nice example of the frequency dependence of the broadband reflectance change -- $\Delta R/R$ gradually decreases with increasing the IR frequency, reaching saturation at about 1800 cm^{-1} . This reflectance decrease is too big and of the wrong sign to be explained with the dielectric properties of the adsorbate. The electronic polarizability of the adsorbate would have a very small effect (about +0.01%) towards increasing the reflectance [29].

The theory which is largely believed to account for the adsorbate induced reflectance change was proposed by Persson and Volokitin [4-6] several years ago. It is based on a concept of “surface resistivity” and attributes the broadband decrease in the reflectance of metals observed upon gas adsorption to the increase of the diffuse scattering of conducting electrons from the adsorbates on the surface. The model predicts the frequency, coverage and temperature dependence of the reflectance change and the relation between $\Delta R/R$ and the resistivity change $\Delta\rho$ of thin films. It also explains antiabsorption resonances observed by reflection absorption IR spectroscopy (RAIRS) [30-33] and effects of atomic scale friction [34]. Lin *et al.* have pointed out that the relationship between the reflectance and resistivity change is pretty general, originating from the fact that both of them are connected to diffuse scattering of conducting electrons from the adsorbate, and does not involve many of the more subtle details of the Persson-Volokitin model [8].

The theory by Persson-Volokitin was inspired by the observation of the remarkable antiabsorption resonances by Reutt et al. [30] and Hirschmugl et al. [31-33], using RAIRS. In contrast to the dipole-allowed vibrational resonances (adsorbate vibrations normal to the surface), the reflectance is actually *increasing* at the resonance frequency, relative to the nearby frequencies (Figure 1-4). They were attributed to molecular

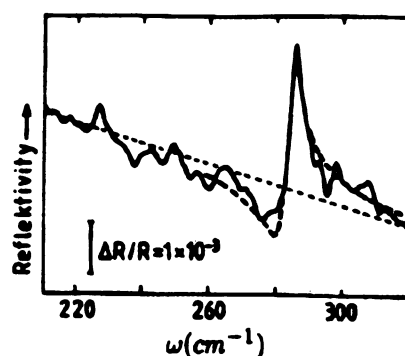


Figure 1-4. Antiabsorption resonance observed by Hirschmugl *et al.* [31] using RAIRS. The absorption of the IR light decreases at the resonance frequency. The graph is reproduced from reference [7].

translations and rotations, parallel to the surface. These are formally dipole-forbidden vibrational modes as the component of the incident light parallel to the surface is orders of magnitude smaller than the normal component and thus cannot couple directly to the adsorbate oscillations.

The originally proposed model uses a local optics approach and is valid for light frequency ω

$$\omega \gg \frac{v_F}{\delta}, \quad (1-12)$$

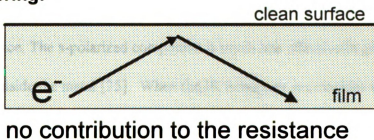
where v_F is the Fermi velocity of the substrate and $\delta = c/\omega_p$ is the classical skin depth, c is the speed of light and ω_p is the plasma frequency. In the local optics approach the conducting electron moves only small distances (on the scale of the decay length δ of the electric field due to the incident light) during one period $T=2\pi/\omega$ of the light. Practically the electron does not see the spatial variation of the electric field and Drude conductivity and local optics apply. The frustrated rotation for CO/Cu(100) discovered by Hirschmugl et al. is at frequency $\omega_o \approx 285 \text{ cm}^{-1}$ and $v_F/\delta \approx 500 \text{ cm}^{-1}$ for copper (Figure 1-4). For this case the condition (1-12) does not hold. For the low light frequencies $\delta < v_FT$ the conducting electron experiences a spatially varying electric field during one period T , requiring non-local treatment. The theory was further expanded [7] to include the non-local effects at lower frequencies using a Boltzmann transport equation approach originally developed to study the anomalous skin effect. This treatment is valid for all IR frequencies which satisfy the condition $\omega \ll \omega_p$. For the light frequency range used in my experiments, the condition (1-12) is well satisfied and both local and non-local treatment give the same results.

Next I will introduce the details of the Persson-Volokitin model:

1. The metal is treated in the semi-infinite jellium approximation - the conducting electrons form a free electron (Drude) gas, characterized with bulk relaxation time τ_B and a mean free path l ($l = v_F\tau_B$).

2. At the surface there is a random distribution of adsorbates with surface density n_a . The conducting electrons experience two types of scattering events at the surface: First, with probability p , not losing momentum parallel to the surface (p is the Fuchs specularity parameter), and second, probability $1-p = n_a\Sigma$, having their parallel momentum randomized due to the adsorbates. Σ is the adsorbate scattering cross section. The first type corresponds to a specular scattering and the second to a diffuse scattering at the surface (Figure 1-5). In the second case all of the momentum change goes to the adsorbate, but not to the lattice or surface defects.

Specular Scattering:



Nonspecular Scattering:

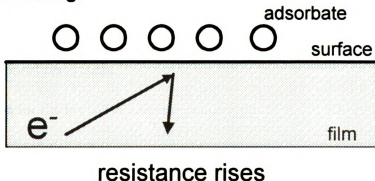


Figure 1-5. Specular and nonspecular scattering of conducting electrons at the surface.

3. Only the *p*-component of the incident light is considered because the resultant of the incident and reflected electric fields for the *s*-polarization is practically zero at metal surfaces due to the close to π phase change. The perpendicular electric field component of the *p*-polarization is orders of magnitude higher than the parallel component at the surface, so *only* the molecular vibrations with a dynamic dipole moment normal to the surface can couple to the incident light - the dipole-allowed vibrational modes. The electric field component parallel to the surface can couple only to the free electrons in the metal, but not to the adsorbate, as is much smaller in magnitude. The broadband absorption occurs *inside* the metal and is caused by diffuse scattering of conduction electrons from the adsorbates. Inside the metal it is the field parallel to the surface that dominates. It comes from the *p*-polarized component of the light, which is strongly refracted at the interface. The *s*-polarized component is much less effective in giving a parallel electric field inside the metal [35]. When the IR frequency ω coincides with the frequency ω_0 of the parallel adsorbate vibrations, the adsorbed molecules move in resonance with the drift motion of the conducting electrons, which results in vanishing of the additional surface resistivity due to diffuse electron scattering from the adsorbates and the reflectance goes back to its value for a clean surface - the dipole-forbidden translational and rotational resonances.

The expression for the fractional reflectance change $\Delta R/R$ for a *p*-polarized light incident at angle θ , which follows from the non-local treatment is pretty complicated [7]:

$$\frac{\Delta R}{R} = -\frac{3(1-p)}{\pi^2 \cos\theta} \frac{\omega^2}{\omega_1 \omega_p} \frac{\operatorname{Re}[G(\omega / \omega_1, l, \delta)]}{1 - \frac{4}{\pi \cos\theta} \frac{\omega}{\omega_p} \operatorname{Im}\left[\int_{-\infty}^{\infty} \frac{dq}{\varepsilon(q, \omega / \omega_1, l, \delta)}\right]}. \quad (1-13)$$

The complex-valued functions G and ε are given by:

$$G = \int_1^{\infty} dy \left(\frac{1}{y} - \frac{1}{y^3} \right) f^2(y) + \frac{4i\eta\omega}{\omega_0^2 - \omega^2 - i\omega\eta} \left[\int_1^{\infty} dy \left(\frac{1}{y^2} - \frac{1}{y^4} \right) f(y) \right]^2, \quad (1-14)$$

where

$$f(y) = \int_{-\infty}^{\infty} dq \frac{1}{\varepsilon(q, \omega, \omega_1, l, \delta)} \frac{1}{1 + i\beta y}, \quad (1-15)$$

and

$$\varepsilon = q^2 - \frac{3i}{4\beta} \frac{\omega}{\omega_1} \left(\frac{\beta}{iq} \right)^3 \left(\left(2 \frac{iq}{\beta} \right) + \left(\left(\frac{iq}{\beta} \right)^2 - 1 \right) \ln \left(\frac{1 + \frac{iq}{\beta}}{1 - \frac{iq}{\beta}} \right) \right), \quad (1-16)$$

where

$$\beta = \frac{\delta}{l} - \frac{i\omega}{\omega_1}. \quad (1-17)$$

The rolloff frequency $\omega_l = v_F/\delta$ specifies the frequency range when the non-local effects become important as discussed above (equation 1-12). The damping coefficient η characterizes the friction force between the adsorbate and free electrons and is related to

the specularity parameter p . Whether or not this coefficient is important for accurately predicting the broadband reflectance change has been discussed in the literature and is still controversial [36,37].

Far from resonances the fractional reflectance change due to surface adsorption is expressed as [38]:

$$\frac{\Delta R}{R} = -\frac{3\nu_F(1-p)}{4c \cos\theta} f\left(\frac{\omega}{\omega_1}, \frac{l}{\delta}\right). \quad (1-18)$$

The fractional broadband reflectance change is negative, meaning that always the clean surface has a higher reflectance. The frequency dependence is incorporated in the function f , which involves properties only of the metal, and approaches unity for frequencies $\omega \gg \omega_1$. The coverage dependence comes from the quantity $(1-p)$. Considering that $1-p = n_a \Sigma$, $\Delta R/R$ is linearly related to the concentration of the adsorbates n_a , if Σ is independent of n_a . The dependence on the temperature is indirect and comes through the expression for the mean free path $l = \nu_F \tau_B$. Both R and ΔR involve l so the temperature dependence is complicated and condition specific.

The earliest reports on adsorbate induced reflectance change are by Riffe, Hanssen and Sievers [39-41] and Reutt, Chabal and Christman [30] who studied a variety of adsorbates on W(100) and Mo(100) crystals. A minimum in the broadband reflectance, observed by Reutt *et al.*, led to the interpretation of an adsorbate-induced surface electronic state.

Different substrates and adsorbates have been considered since then. The frequency dependence of the broadband reflectance change and the antiabsorption resonances observed by Hirschmugl *et al.* [31-33] for CO / Cu(100) and (111) are in excellent agreement with the mechanism proposed by Persson. Lin *et al.* reported very good agreement with the scattering theory for the frequency dependence of the broadband reflectance change for O adsorption on Cu(100) [8,28]. The solid line in Figure 1-3, reproduced from their paper, represents a fit to the Persson-Volokitin scattering theory. Obviously the agreement is pretty convincing.

Measurements of the coverage, temperature, and frequency dependence of the broadband reflectance change induced by CO on Pt(111), by Kuhl *et al.* supported the validity of the scattering model [38]. Lamont *et al.* detected the antiabsorption peaks due to dipole-forbidden parallel vibrations of H and D on Cu(111) [42]. A discrepancy with the theory was found for the frequency dependence of the broadband reflectance change of H/Cu(111) for frequencies higher than 1000 cm^{-1} , but was attributed to electronic excitations involving adsorbate induced surface states, similar to what was proposed for the case of H on W(100) and Mo(100) [30]. Borguet *et al.* reported a linear increase of the reflectance change with coverage, in agreement with the model, both for near-infrared and visible light [43,44].

To summarize the above experimental review I want to emphasize that a good deal of evidence in support of the Persson-Volokitin scattering model has been accumulated in the recent years.

1-4. Relation Between the Adsorbate-Induced Broadband IR Reflectance and DC Resistivity Change of Thin Metal Films

The main goal of my study is the experimental examination of the linear relationship, predicted by the scattering model, between the fractional reflectance change $\Delta R/R$ and resistivity change $\Delta\rho$ for well characterized epitaxial Cu(100) thin films. In this chapter I will develop in detail the above relationship closely following the derivation by Lin *et al.* [8]. This derivation is based on the Persson-Volokitin model but does not involve its more subtle and speculative details like damping of the adsorbate translations and rotations parallel to the surface. It demonstrates that the relationship between reflectance and resistivity is pretty general and the connection to the antiabsorption resonances and frictional damping comes from the fact that all of the above effects involve electron scattering. The final result for the relationship between broadband reflectance and resistivity change, far from resonances, is the same with or without considering atomic friction and vibrational damping. Even if antiabsorption resonances come from another mechanism the relationship between $\Delta R/R$ and $\Delta\rho$ is still valid.

To account for surface effects on reflectance, non-local corrections to the classical Fresnel formulas are added using Feibelman's d -parameter formalism [45]. The fractional reflectance change of p -polarized light due to change in the surface conditions is expressed as[8]:

$$\frac{\Delta R}{R} = -\frac{4\omega}{c} \frac{\text{Im}(d_1)}{\cos\theta}, \quad (1-19)$$

where ω is the light frequency, c is the velocity of light, θ is the incident angle. Equation (1-19) is valid provided that $|\varepsilon| \gg (1/\cos^2 \theta) \gg 1$, ε is the complex local dielectric function of the metal. The parameter d_{\parallel} is given by:

$$d_{\parallel} = \frac{\int z \left(\frac{\partial \sigma_{\parallel}}{\partial z} \right) dz}{\int \left(\frac{\partial \sigma_{\parallel}}{\partial z} \right) dz}, \quad (1-20)$$

where z is the direction normal to the surface and σ_{\parallel} is the parallel component of the complex conductivity for a uniform electric field. $\text{Im}(d_{\perp})$ is negligible compared to $\text{Im}(d_{\parallel})$, because of the strong refraction experienced by the incident light in the metal.

The Persson-Volokitin theory proposes a slab model: Deep in the metal the conductivity has its bulk value σ_B , while near the surface it is affected by the randomly distributed adsorbates and can be expressed as:

$$\sigma_s(\omega) = \sigma_B(\omega) + \Delta\sigma(\omega) \quad (1-21)$$

The near-surface region where (1-21) is valid is of the order of the electron elastic mean free path $l_B = v_F \tau_B$. Using the above model to calculate d_{\parallel} the expression for the fractional reflectance change for p -polarized light becomes:

$$\frac{\Delta R}{R} = \frac{4\omega l_B/c}{\cos\theta} \text{Im} \left[\frac{\Delta\sigma(\omega)}{\sigma_B(\omega)} \right]. \quad (1-22)$$

As previously discussed, provided that equation (1-12) is valid for the particular material and light frequency range, a local description of the metal's dielectric response can be used. For copper $v_F/\delta=310 \text{ cm}^{-1}$, the light frequency used in my study is well above 2000 cm^{-1} , so the condition (1-12) is satisfied. The bulk conductivity, using the Drude free electron gas approximation, is given by:

$$\sigma_B(\omega) = \frac{ne^2\tau_B}{m(1-i\omega\tau_B)}, \quad (1-23)$$

Here n is the conducting electron density, m is the electron effective mass, and e is the electron electric charge. As the adsorbates can affect both the conducting electron density n and the scattering time τ the change in the conductivity $\Delta\sigma$ in the near surface region can be expanded to first order in changes Δn and $\Delta\tau$.

$$\frac{\Delta\sigma(\omega)}{\sigma_B(\omega)} = \frac{\Delta n}{n_B} + \frac{\Delta\tau}{\tau_B(1-i\omega\tau_B)}. \quad (1-24)$$

In the above expression only the term in $\Delta\tau$ has a imaginary part, which can result in reflectance change (formula 1-22). The term in Δn would produce only a resistivity change. The scattering hypothesis assumes that the main reason for the experimentally

observed resistivity and reflectance change of metals due to gas adsorption is the diffuse scattering of conducting electrons from the adsorbates. No change in the conducting electron density n is presumed. Therefore the term $\Delta n/n_B$ in (1-24) can be neglected. For a film of thickness l_B , and $\omega \gg 1/\tau_B$, $\text{Im}(\Delta\sigma(\omega))$ can be expressed using the dc resistivity $\rho = 1/\sigma(\omega = 0)$ as:

$$\text{Im}\left[\frac{\Delta\sigma(\omega)}{\sigma_B(\omega)}\right] = -\frac{1}{\omega\tau_B} \frac{\Delta\rho(l_B)}{\rho_B}. \quad (1-25)$$

As it is well established experimentally that $t\Delta\rho$ does not depend on the film thickness t [18,20], the reflectance change can be related to the dc resistivity change for arbitrary film thickness:

$$\frac{\Delta R}{R} = -\frac{4l_B}{c\tau_B \cos\theta} \frac{\Delta\rho(l_B)}{\rho_B} = -\frac{4}{c\rho_B\tau_B \cos\theta} [t\Delta\rho(t)]. \quad (1-26)$$

Using:

$$\rho_B\tau_B = \frac{m}{ne^2}, \quad (1-27)$$

equation (1-26) becomes:

$$\frac{\Delta R}{R} = -\frac{ne^2}{mc} \frac{4}{\cos\theta} [t\Delta\rho(t)] \quad (1-28)$$

This is the main equation to be tested in my investigation. Several important points should be emphasized:

1. For the frequency region $\omega \gg v_F/\delta$, $\omega \gg 1/\tau_B$, where equation (1-28) is valid the fractional reflectance change does not depend on the frequency;
2. The reflectance change is linearly proportional to the resistivity change and the proportionality coefficient does not depend on the adsorbate, but only on bulk parameters of the metal;
3. The electron density n is assumed to be constant;
4. $\Delta R/R$ does not depend on the film thickness t , for $t \gg \delta$.

The relationship (1-28) was first tested experimentally by Lin *et al.* [8]. They measured the fractional reflectance change for O and CO on a Cu(100) single crystal and for CO on a Ni(100) single crystal and compared their results to published resistivity change measurements for the corresponding thin-film systems. Their results are summarized in Table 1-1.

For CO and O adsorption on Cu the experimental and calculated values for $\Delta R/R$ are within factor of 2 and were considered consistent with the scattering model within the experimental error due to uncertainty in the published resistivity data. However for CO on Ni the experimental reflectance change was a factor of 30 smaller than the predicted one using the values for $t\Delta\rho$ found in the literature. Lin *et al.* point out that the above experiments cannot serve as a definite quantitative test of the scattering model as

Table 1-1. Adsorbate induced fractional reflectance change $\Delta R/R$ for adsorbate coverage n_a measured experimentally and calculated using equation 1-28 and published values for $t\Delta\rho$. The table is reproduced from reference [8].

System	n_a (10^{14}cm^{-2})	$(t\Delta\rho)$ ($10^{-12}\ \Omega\text{cm}^2$)	$(\Delta R/R)_{calc}$ (%)	$(\Delta R/R)_{exp}$ (%)
CO/Cu(100)	6.1	0.60	-2.2	-1.1±0.2
O/Cu(100)	3.8	0.42	-1.5	-1.1±0.2
		0.70	-2.6	
CO/Ni(100)	6.4	1.47	-5.8	-0.2±0.2

the resistivity and reflectance measurements were taken on different samples under different conditions, and a rigorous test would involve simultaneous resistivity and reflectance measurements of well characterized epitaxial films.

Recently Hein and Schumacher reported simultaneous reflectance and resistivity change measurements of *in situ* grown thin polycrystalline films on glass substrates, using unpolarized IR light [46]. The systems studied were O, CO, Cu on Cu thin films and Ag on Ag thin films. The linearity between resistivity and reflectance change predicted by the

scattering model was confirmed, but quantitative discrepancies for the actual slope were found (Table 1-2).

The observed quantitative discrepancy was not explained but the authors emphasized that it cannot be attributed to uncertainties in the experimental parameters. It was also pointed out that the theoretical calculations deal with a semi-infinite jellium model, while the films were polycrystalline with grain size of the order of the film thickness.

Table 1-2. Comparison of the theoretical and experimental values for the slope of the linear dependence between reflectance change and DC resistivity change for different adsorbates on Cu and Ag polycrystalline films. The table is reproduced from the study by Hein and Schumacher [46].

System	$(\Delta R/\Delta\rho)_{\text{calc.}}$ $(\mu\Omega \text{ cm})^{-1}$	$(\Delta R/\Delta\rho)_{\text{exp.}}$ $(\mu\Omega \text{ cm})^{-1}$
O/Cu	-0.0085	-0.030
CO/Cu	-0.0077	-0.014
Cu/Cu	-0.0085	-0.010
Ag/Ag	-0.0082	-0.025

My work presents a test of the relationship (1-28) for oxygen and formate adsorption on epitaxial Cu(100) thin films, grown *in situ* in UHV, and carefully characterized. In Chapter 4 I will discuss the preparation and characterization of the samples. In Chapter 5 the actual combined reflectance and resistivity change

measurements are presented and analyzed. The predicted linearity between reflectance and resistivity change was found for oxygen, but for the formate no detectable reflectance change together with a significant resistivity change was observed in striking contrast to the predictions of the scattering model. Thus the present study is the first test of the Persson-Volokitin scattering theory on well characterized epitaxial thin films and the first work clearly demonstrating deviation from the model, for the particular system formate on Cu(100).

References

- [1] I. J. Langmuir, *Am. Chem. Soc.*, **38**, 2221 (1916).
- [2] Ralf Vanselow, *Chemistry and Physics of Solid Surfaces*, CRC Press, Boca Raton, Florida (1979).
- [3] J. E. Lenard-Jones, *Trans. Faraday Soc.*, **28**, 223 (1932).
- [4] B.N.J. Persson, *Phys. Rev. B* **44**, 3277 (1991).
- [5] B.N.J. Persson, *Chem. Phys. Letters* **185**, 292 (1991).
- [6] B.N.J. Persson, *Chem. Phys. Letters* **197**, 7 (1992).
- [7] B.N.J. Persson and A.I. Volokitin, *Surface Sci.* **310**, 314 (1994).
- [8] K.C. Lin, R.G. Tobin, P. Dumas, C.J. Hirschmugl and G.P. Williams, *Phys. Rev. B* **48**, 2791 (1993).
- [9] C.-A. Chang, *Phys. Rev. B* **42**, 11 946 (1990).
- [10] C.-A. Chang, *Surf. Sci.* **237**, L421-L423 (1990).
- [11] C.-A. Chang, *J. Appl. Phys.* **68**, 5893 (1990).
- [12] C.-A. Chang, *J. Vac. Sci. Technol. A* **8**, 3779 (1990).
- [13] C.-A. Chang, *J. Vac. Sci. Technol. A* **9**, 98 (1991).
- [14] Y.-T. Cheng, Y.-L. Chen, M.M. Karmarkar and W.-J. Meng, *Appl. Phys. Lett.* **59**, 953 (1991).
- [15] Y.-L. Chen and Y.-T. Cheng, *Mat. Lett.* **15**, 192 (1992).
- [16] Y.-T. Cheng and Y.-L. Chen, *Appl. Phys. Lett.* **60**, 1951 (1992).
- [17] R.Naik, M. Ahmad, G.L.Duifer, C.Kota, A.Poli, Ke Fang, U. Rao and J.S. Payson, *J. Magnetism and Magnetic Mat.* **121**, 60 (1993).
- [18] P. Wissmann in: *Surface physics*, ed. G. Höhler, Springer Tracts in Modern Physics, **77**, Springer, New York, (1975).

- [19] D. Dayal, H.-U. Finzel and P. Wissmann in: *Thin metal films and gas chemisorption*, ed. P. Wissman Elsevier, Amsterdam, (1987).
- [20] D. Schumacher, *Surface scattering experiments with conduction electrons*, ed. G. Höhler, Springer Tracts in Modern Physics, **128**, Springer, New York, (1993).
- [21] K. Fuchs, Proc. Camb. Phil. Soc. **34**, 100 (1938).
- [22] E.H. Sondheimer, Adv. Physics **1**, 1 (1952).
- [23] J. Vancea, H. Hoffmann, Thin Solid Films, **92**, 219 (1982).
- [24] J. Vancea, H. Hoffmann, K. Kastner, Thin Solid Films, **121**, 201 (1984).
- [25] Y. Namba, Jpn. J. Appl. Phys., **9**, 1326, (1970).
- [26] R. Suhrmann, K. Schulz, Z. Phys. Chem. (Frankfurt) **1**, 69 (1954).
- [27] W.M.H. Sachtler, G.J.H. Dorgelo, Z. Phys. Chem. (Frankfurt) **25**, 69 (1960).
- [28] K.C. Lin, R.G. Tobin and P. Dumas, Phys. Rev. B **49** (1994) 17273 (1994); **50**, 17760 (1994).
- [29] R.G. Tobin, Phys. Rev. B **45**, 12110 (1992).
- [30] J.E. Reutt, Y.J. Chabal and S.B. Christman, Phys. Rev. B **38**, 3112 (1988).
- [31] C.J. Hirschmugl, G.P. Williams, F.M. Hoffmann and Y.J. Chabal, Phys. Rev. Letters **65**, 480 (1990).
- [32] C.J. Hirschmugl, Y.J. Chabal, F.M. Hoffmann and G.P. Williams, J. Vac. Sci. Technol. A **12**, 2229 (1994).
- [33] C.J. Hirschmugl, G.P. Williams, B.N.J. Persson and A.I. Volokitin, Surface Sci. **317**, L1141 (1994).
- [34] J. Krim, D.H. Solina and R. Chiarello, Phys. Rev. Letters **66**, 181 (1991).
- [35] Y.J. Chabal, Surface Science Reports, **8**, 211 (1988).
- [36] R.G. Tobin, Phys. Rev. B **48** 15468 (1993).
- [37] B.N.J. Persson, Phys. Rev. B **48** 15471 (1993).

- [38] D.E. Kuhl, K.C. Lin, Chilhee Chung, J.S. Luo, Hong Wang and R.G. Tobin, *Chemical Physics* **205**,1 (1996).
- [39] D.M. Riffe, L.M. Hanssen and A.J. Sievers, *Phys. Rev. B* **34**, 692 (1986).
- [40] D.M. Riffe, L.M. Hanssen and A.J. Sievers, *Surface Sci.* **176**, 679 (1986).
- [41] D.M. Riffe and A.J. Sievers, *Surface Sci.* **210**, L215 (1989).
- [42] C.L.A Lamont, B.N.J. Person and G.P. Williams, *Chem. Phys. Lett.* **243**, 429 (1995).
- [43] E. Borguet, J. Dvorak, and H.-L. Dai, *Laser Techniques for Surface Science, Proceedings of the Society of Photo-Optical Instrumentation Engineers, Volume 2125* ,12 (1994).
- [44] J. Dvorak, E. Borguet, and H.-L. Dai, *Surface Science Letters*, **369**, L122 (1996)
- [45] P.J. Feibelman, *Prog. Surf. Sci.* **12**, 287 (1982).
- [46] M. Hein and D. Schumacher, *J. Phys. D* **28**, 1937 (1995).

Chapter 2

Apparatus and Experimental Technique

In order to perform my combined resistivity and broad-band reflectance measurements on Cu(100) epitaxial films, I had to modify the existing infrared spectroscopy system to allow *in situ* growth of thin films in ultrahigh vacuum (UHV) conditions. The UHV surface analysis chamber had to be furnished with thin film evaporation equipment, which I will discuss in this chapter, and a fast sample-entry load-lock system together with a new sample mount which is described in detail in chapter 3.

The design, construction and testing of these new facilities took a considerable amount of time and work but it is a very important addition to our system allowing us to study freshly grown thin films on different substrates. In this chapter I will also describe our far-infrared surface spectroscopy system and the techniques for measuring broad-band reflectance and film resistivity changes used in my investigation.

2-1. Far-infrared surface spectroscopy system

The layout of our far-infrared surface spectroscopy system is shown in Figure 2-1, which is reproduced from reference [1]. The infrared (IR) light is generated and

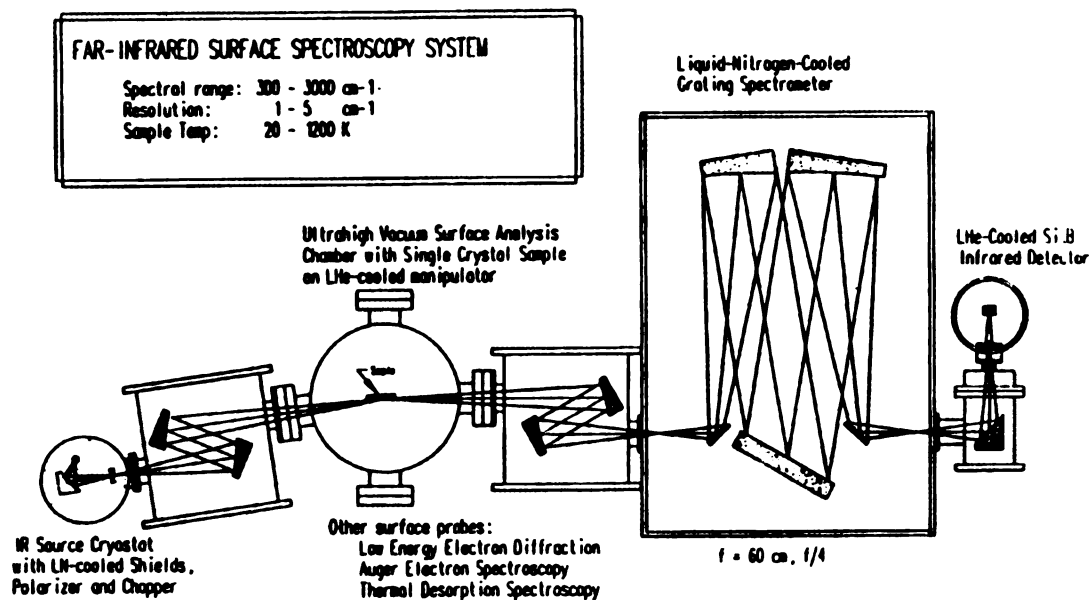


Figure 2-1. Layout of the far infrared surface spectroscopy system. Reproduced from reference [1] by C. Chung.

modulated in a source cryostat and via transfer optics is directed at a grazing angle towards the sample. The sample is located in the UHV surface analysis chamber, which is the only component of the system operating under ultra high vacuum conditions. The rest of the components are kept under high vacuum ($10^{-6} - 10^{-8}$ Torr) After reflecting from the sample the IR light passes through another set of transfer optics and enters the home-built Czerny-Turner grating spectrometer. Part of the IR light with the particular frequency and polarization of interest exits the spectrometer and via a third set of transfer optics is directed towards the IR detector. There the optical signal is transformed to a voltage using a photoconductor, amplified and after that registered by a lock-in amplifier (LIA), connected to a computer. Parallel with monitoring of the reflectance, the sample

resistance is registered via a four-wire resistivity measurement, and the sample temperature is determined using a thermocouple. The process of data acquisition is automated using home made software. Having described the general plan and operation of our system, next I will discuss in more detail its main components.

2-1-1. Optical setup

The IR light is generated by a conventional silicon-carbide globar, resistively heated to 1300 K. It is situated in one of the focal points of a gold plated adjustable ellipsoidal mirror. Gold plated mirrors are used through the system because of their superior reflectance performance in the IR range compared to other types of mirrors. A tuning fork chopper [2] is located in the second focal point of the ellipsoidal mirror. It modulates the intensity of the IR light at 800 Hz. This frequency was chosen to avoid mechanical resonances with other system components. The above elements, except the globar, are kept at liquid nitrogen (LN) temperature as they are mounted on a copper plate, in contact with a LN reservoir. This is in order to minimize the background photon flux modulated by the chopper and sent to the successive elements of the system. The whole assembly is kept at high vacuum (HV) to eliminate atmospheric absorption of the IR light and help keeping the optical elements cold.

After the chopper the IR light is directed towards transfer optics (TO), which shares the same vacuum space with the source elements, but is kept at room temperature. There is no need of cooling, because the TO is after the chopper on the optical path. The TO consists of two off-axis paraboloidal mirrors, one of which is adjustable from outside

of the vacuum chamber. The purpose of the transfer optics is to produce a 1.8 times magnified image of the chopper at the sample in order to illuminate the whole sample area and the reflected light to be collected by a spectrometer with a focal number $f/4$. Through a differentially pumped CsI [3] window the IR light hits the sample, located in the main UHV chamber. The angle of incidence is 86° . The reflected portion enters the second transfer optics via another CsI window. CsI is chosen because of its high transmission in the infrared, but it must be handled very carefully, because it is easily damaged if exposed to high humidity conditions. The second transfer optics is a mirror image of the first. It demagnifies the image of the chopper, reflected by the sample, and places it on the entrance slit of the spectrometer.

The home-built grating spectrometer is the most complicated optical subsystem of the apparatus. It operates under high vacuum and is cooled to LN temperature. All the elements are mounted on an aluminum plate, kinematically supported via three invar rods. The aluminum plate is clamped to the outer shell of the spectrometer for mechanical stability and connected to a LN reservoir, carefully designed to provide adequate cooling. The IR radiation reflected from the sample first encounters the entrance slit. There is a choice of several slits, mounted on a rotatable wheel, allowing change in the resolution of the spectrometer from outside. Via a folding mirror the light is directed towards the collimating mirror (off-axis paraboloid) and the collimated beam is diffracted by a gold plated grating [4]. Three different gratings are used to cover the spectral range of 300 to 3000 cm^{-1} . Only one grating can be installed at any given time and the spectrometer must be opened in order to replace a grating. The diffracted light is next collected by a camera

mirror (also off-axis paraboloid) and via a second folding mirror sent to a polarizer (a gold wire grid on a silver bromide substrate [5]) Via the exit slit the p-polarized component of the light is directed towards a third set of transfer optics. Similar to the entrance slit assembly, a variety of exit slits could be chosen externally and different low-pass IR filters are provided to cut higher diffraction orders.

The third set of transfer optics shares the same vacuum space with the spectrometer and is LN cooled by its own LN reservoir. The main element is an adjustable ellipsoidal mirror, having as its two focal points the exit slit of the spectrometer and the detector.

The IR detector is a boron doped silicon photoconductor (Si:B), 1x1x0.4 mm in size and operated at liquid helium temperature. It is mounted at the exit aperture of a gold plated Winston cone - a paraboloidal conical device permitting all the light entering its larger entrance aperture (10 mm in our case), via successive wall reflections to exit through the smaller exit aperture (1mm in diameter). The whole detector assembly is installed in a commercial liquid helium dewar [6].

The electrical signal from the detector is boosted by a two stage transimpedance amplifier. The first stage consists of two JFETs with two switchable feedback resistors (1M Ω and 60 M Ω), mounted on the cold plate of the detector dewar. The two transistors are heated to 77K to allow normal operation. The second stage is an AC coupled operational amplifier with a switchable gain (2 and 10), operating at room temperature.

2-1-2. Main UHV chamber

The main UHV chamber, which houses the sample, is located in between the two transfer optics. As discussed in the introduction ultrahigh vacuum (UHV) is the only acceptable environment for a modern surface science experiment, granting several hours before the specimen surface is contaminated by the ambient gases. The UHV chamber, 12" (30.5cm) in diameter and 25" (98.4 cm) in height, is custom-made out of stainless steel. A large number of flanged ports is provided for mounting a variety of equipment. It is divided into three levels: IR/sample transfer and evaporation (IR/STE) on the bottom, surface analysis in the middle and precision X-Y-Z- θ manipulator [7] on the top. The sample mount is attached to a LN reservoir (cold finger), which is mounted on the manipulator. The middle surface analysis level houses equipment for low energy electron diffraction (LEED), Auger electron spectroscopy (AES), an ion sputtering gun and a residual gas analyzer with a temperature programmed desorption (TPD) capability.

The bottom IR/STE level is used to perform the reflectance measurement, sample introduction and thin film growth. It is equipped with a fast-entry load-lock system (FELLS) and thin film evaporation equipment. The design and construction of these two systems was a considerable part of my project. The FELLS is described in detail in chapter 3. The thin film evaporation system consists of a resistive evaporator and a crystal thickness monitor. The evaporator is built on a standard 4.5" (11.4 cm) flange. There are two filaments shielded from each other, providing the capability of evaporating two different metals. A rotating shutter is available to block one of the filaments at a time. The whole assembly is enclosed in an oxygen free high conductivity (OFHC) copper

sleeve, tightly fit over a stainless steel reservoir for a cooling liquid. The copper sleeve consists of two shells for easy removal and installation. A flow of liquid nitrogen or chilled water can be used to provide the cooling. Cooling during the evaporation is essential, as warming of the chamber surfaces would result in a pressure increase, which is highly undesirable. A chimney-shaped shield is attached to the copper sleeve in order to direct evaporation only towards the sample and the crystal monitor, thus protecting the rest of the chamber. A stainless steel shield on the sample mount also helps prevent evaporation on unwanted areas. The evaporator flange is mounted on a bellows-sealed linear translator so the evaporator assembly (EA) can be retracted and separated from the main UHV chamber, using a gate valve. This option permits us to change filaments without breaking the UHV in the main chamber. Before reintroducing the EA to the chamber the space of the linear translator is pumped to high vacuum using a turbo-molecular pump. Baking of the EA for a couple of hours before reintroducing helps to reduce the pressure spike in the main UHV chamber.

Achieving of UHV after the chamber has been vented to atmospheric pressure is a lengthy procedure taking about 72 hours. Once sealed, the chamber is rough pumped using molecular sorption and turbo-molecular pumps. When the pressure gets down in the 10^{-6} Torr range the main ion pump [8], supplemented with a titanium sublimation pump, is opened to the chamber. The next step is a 36– to 48– hour bakeout at about 100 to 110 °C. It is accomplished by heating tapes, placed all around the chamber, together with an internal IR heater. During the bakeout the chamber is wrapped in aluminum foil, helping to keep more even heat distribution. The temperature is monitored by numerous

thermocouples positioned at various locations. After cooling down to a room temperature a base pressure of about $5-7 \times 10^{-11}$ Torr is achieved.

The sample could be exposed to variety of gases via two leak valves. Backfilling of the UHV chamber or a specially designed multihole effusive doser array [9] is used. The doser provides 16 times flux enhancement over the backfilling. The doser is mounted on a bellows-sealed linear translator and is usually retracted far from the center of the UHV chamber when it is not in use. This permits unobstructed maneuvering of the sample holder around the UHV chamber.

2-2. Thin film sample preparation

The samples used in my study are epitaxial *in situ* grown Cu(100) thin films, on Si(100) substrates. The technique for growing of the films was developed using a separate HV evaporator. A detailed study of the surface morphology and electrical characteristics of these films is presented in Chapter 4. Once our UHV chamber was equipped with sample transfer and evaporation equipment we were able to grow the films in UHV conditions. The films grown at UHV are epitaxial and show equivalent or lower surface roughness than the films grown in HV.

Before being introduced into the UHV chamber the silicon sample (2.5 x 1 cm) is first cut out of standard 3" Si wafer (B-doped, 20-50 Ω cm resistivity). It is degreased in a 15 minute ultrasonic bath of acetone followed by methanol. In a separate HV evaporator 150 nm thick silver on top of 10 nm chromium is evaporated on the two ends of the Si chip, using a mask made out of aluminum foil. This way the two contact stripes

are formed. A batch of samples (20 or more) could be processed at the same time, thus increasing the productivity. The Si sample is etched in a 10% aqueous solution of hydrofluoric acid (HF) for about 60 seconds. This treatment removes the SiO₂ and passivates the surface by saturating the Si dangling bonds with hydrogen [10-13]. The sample is then rapidly mounted to a sample disk and introduced into the UHV chamber using the fast sample entry system, discussed in detail in Chapter 3.

As our UHV chamber is equipped with Auger spectroscopy (AES), I was able to investigate the film-growing conditions that provide the cleanest film surfaces. As mentioned before a surface as clean as possible is of crucial importance for a surface science experiment. This kind of studies were not performed for the films grown at high vacuum. It proved that annealing the Si chip for about 15 minutes at 720 to 750 K, after introducing to the UHV chamber, dramatically improves the surface purity of the film grown afterwards. Figure 2-2 presents a comparison between the AES scans for two Cu films grown without and with preannealing of the Si substrate. The top scan (Figure 2-2a), taken from a Cu film grown on a Si chip that was not annealed, reveals substantial amounts of carbon and oxygen present on the surface - about 23 atomic percent C and 3 atomic percent O. The bottom graph (Figure 2-2b) is for a Cu film grown on a Si substrate preannealed at 750 K. The C and O peaks are much smaller and almost indistinguishable from the noise – the contamination of the film surface is reduced to 3 atomic percent C and less than 1.5 atomic percent O.

The positive effect of substrate annealing on the surface purity of our films is attributed to the following. The hydrogen-passivated Si surface is contaminated with

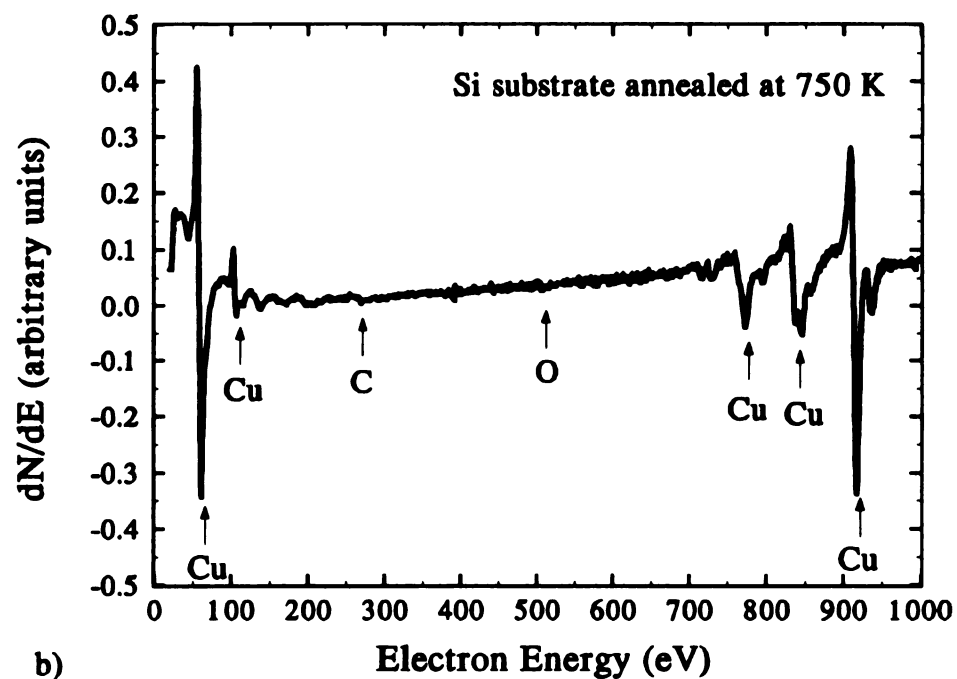
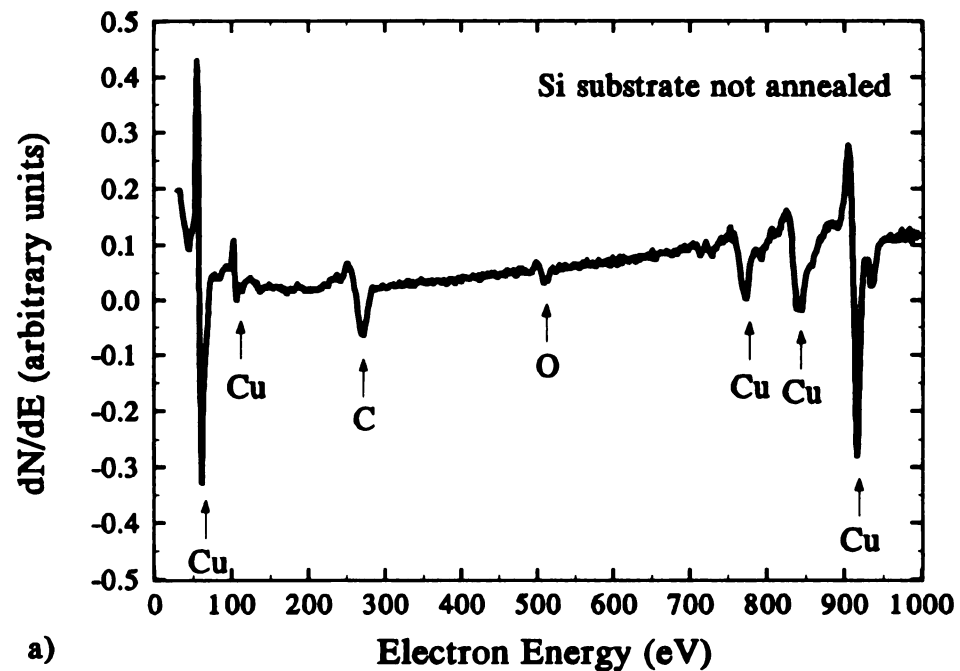


Figure 2-2. Comparison between AES scans for Cu films grown on not annealed (a) and annealed at 750K (b) Si substrate. The surface of the not annealed film is contaminated with about 23 atomic percent (a.p.) C and 3 a.p. O. The surface of the film grown on annealed Si substrate is much cleaner with C and O peaks comparable to the noise level.

carbons from the atmosphere during loading of the sample into the UHV chamber. During and after the film growth the carbons penetrate through the film and show on the surface. This assumption is supported from the fact that for a not annealed substrate the C peak grows significantly with time, which was not observed for films grown on annealed substrates. The annealing of the Si chip causes contamination (water and carbons) to leave the substrate resulting in a much cleaner film surfaces. It also removes the hydrogen passivating the surface, so the film evaporation should be done immediately after the annealing.

Before annealing of the Si chip, the cold finger is filled with liquid nitrogen. This keeps cool the engaging stainless steel springs of the sample transfer mechanism during the heating, thus preventing them from collapsing. It also facilitates cooling down the Si substrate after the annealing as the best films are grown at room temperature (see Chapter 4). In about 30 to 45 minutes the temperature of the Si chip drops to about 300 K. The temperature is kept steady by running the sample heater, which compensates for the heat lost to the cold finger. The films are grown at evaporation rates of 0.1 to 0.2 nm/s to thickness of about 50 nm. During the deposition the pressure in the chamber usually rises and stays in the range 3×10^{-10} to 9×10^{-10} Torr. No post-deposition annealing is performed as it does not improve the surface quality (Chapter 4).

2-3. Combined Resistivity and Broadband Reflection Change Measurement of Thin Cu(100) Films Due to Gas Adsorption

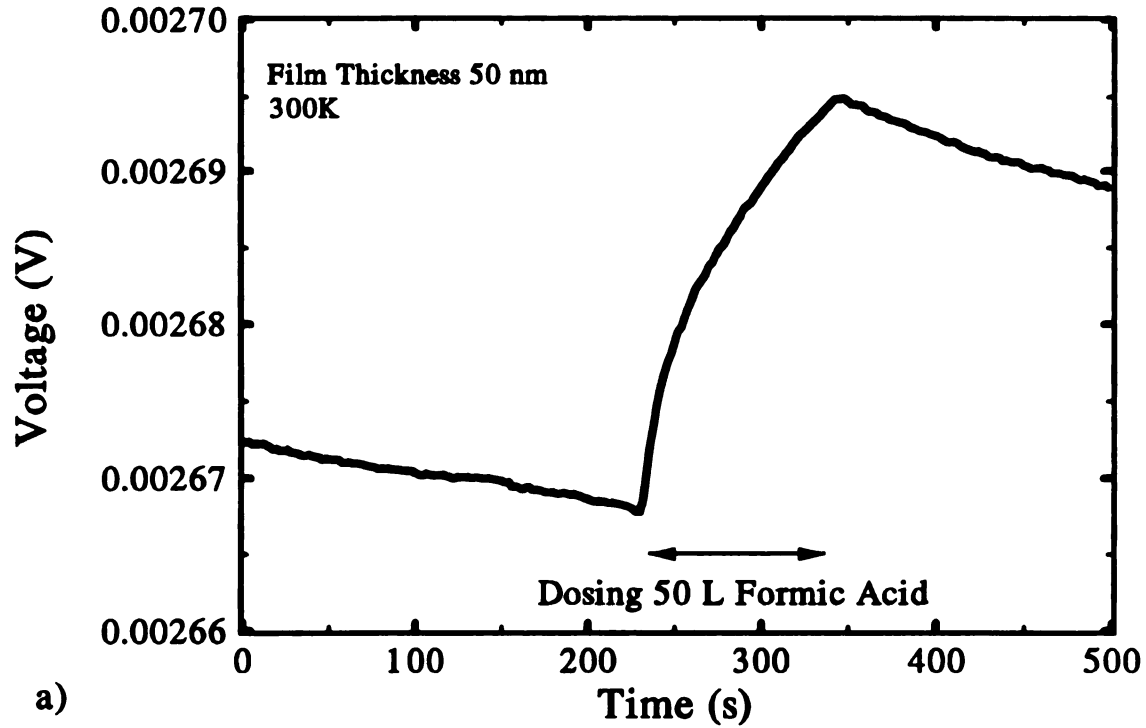
Once the Cu film is grown, the desired temperature has stabilized and the pressure has gone down to $\leq 1 \times 10^{-10}$ Torr, the sample holder is moved to the infrared position. A so-called “time scan” is started by simultaneously monitoring the film’s resistivity and reflectance at fixed time intervals. It is important to measure the clean film for a long enough time in order to establish a stable baseline before a particular gas is introduced into the chamber. The gas is introduced by setting one of the leak valves at a fixed flow, while pumping is kept on. A constant pressure is held in the chamber, as monitored by a nude ionization gauge. After a certain period of time the leak valve is closed and the gas is pumped out. Following the dosing the measurement is continued long enough to establish a new stable baseline. The exposure is determined by taking into account the pressure and the time interval the gas was present in the chamber and is measured in Langmuirs ($1\text{L} = 1 \times 10^{-6}$ Torr s). The change or absence of a change in the sample resistivity and reflectance is registered. Usually the duration of a time scan is between 300 and 800 seconds. Further in this chapter I will discuss in more detail the resistivity and broadband reflectance change measurement.

2-3-1. Resistivity Change Measurement

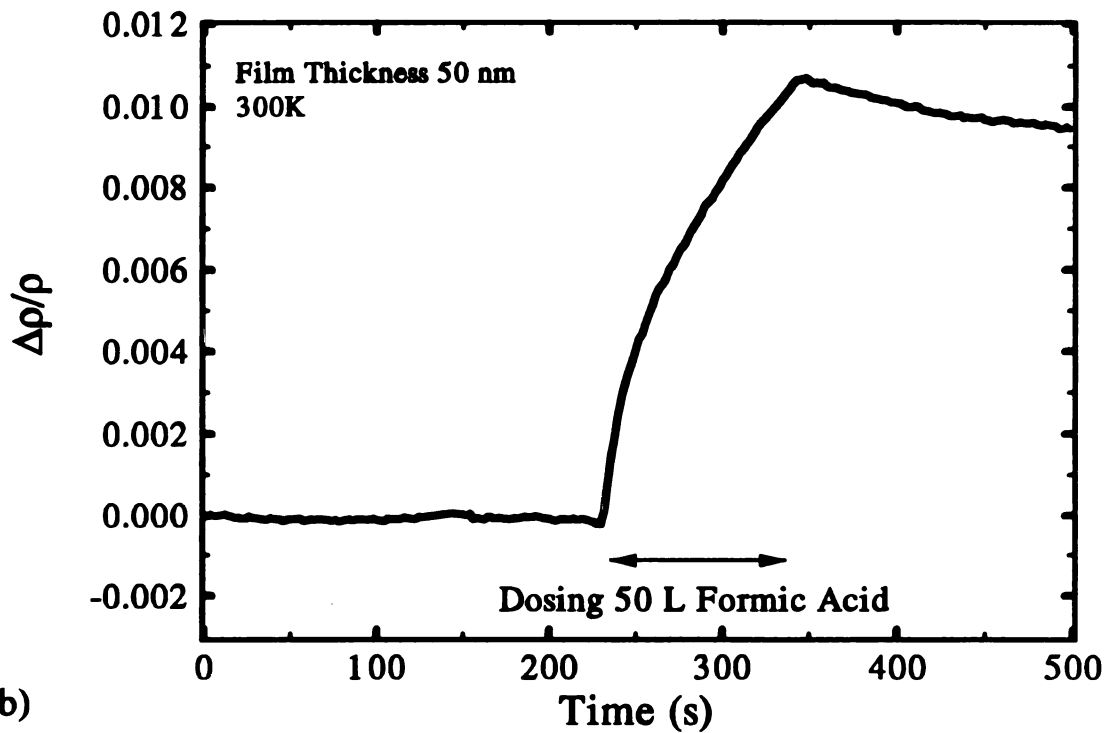
The film resistance is measured by a four-wire ac technique using a 1.0 mA current provided by the internal reference of a lock-in amplifier (LIA) [14], and modulated at 3 kHz. Four breakable electrical contacts to the sample and a thermocouple are provided by

the custom designed sample holder, discussed in detail in Chapter 3. The voltage drop across the sample is registered by the LIA, using two coax cables, with their shields grounded. The LIA measures the difference between the two leads, thus avoiding noise common to both wires. The capacitive and inductive pickup in the leads is less than 8×10^{-9} V/ $\sqrt{\text{Hz}}$ [15]. The data is collected by a computer connected to the LIA, using home made software. The measurement is very low-noise and fractional resistance changes $\Delta V/V < 10^{-4}$ are easily measurable.

A typical resistivity change measurement for a 50 nm thick Cu(100) film at room temperature is presented in figure 2-3. The raw data (figure 2-3a), is the voltage drop across the sample, registered by the LIA. At about the 230th second formic acid gas is introduced in the chamber. The exposure is 50 Langmuirs - 5×10^{-7} Torr for 100 seconds. The linear drift in the baseline is caused by a slight change in the sample temperature during the measurement. To remove the systematic drift from the measurement a line is fitted to the raw data between the 0th to 225th second. This line is subtracted from the raw data and the resulting data is plotted in figure 2-3b. The fractional resistivity change $\Delta\rho/\rho$ caused by the gas exposure is about 1.1% in this case. The absolute resistivity change $\Delta\rho$ is calculated taking into account the film dimensions (thickness, length and width) and the actual resistance of the sample, measured separately. After the end of the dose a slight decrease in the resistance is observed, which is most likely caused by some of the gas leaving the film surface.



a)



b)

Figure 2-3. Resistivity change of Cu(100) film due to 50L formic acid exposure - a) raw data - voltage drop across the sample, registered by the LIA, b) the linear baseline is removed and the fractional resistivity change $\Delta\rho/\rho$ calculated. The maximum $\Delta\rho/\rho$ is about 1.1%.

2-3-2. Broadband Reflectance Change Measurement

The broadband reflectance measurement is performed with the spectrometer cooled to LN temperature in order to reduce the background IR radiation from walls and other surfaces in the spectrometer. The detector is set to a high feedback resistor. The first step is to maximize the IR reflection from the film surface by fine adjusting the sample position and the mirrors of the transfer optics. The spectrometer is set to the desired fixed IR frequency (far from resonances caused by molecular vibrations). The signal modulated by the chopper is registered by a lock-in amplifier using the chopper reference. The data is recorded by a computer.

A typical broad-band reflectance change measurement for a 50 nm thick Cu(100) film due to oxygen adsorption is shown in figure 2-4. A linear baseline has been removed. Beginning at about the 210th second the film is exposed to 50 Langmuirs of oxygen (5×10^{-7} Torr for 100 seconds). The reflectance of the sample drops sharply and reaches a saturation before the end of the dosing. The total broadband fractional reflectance change is about 0.5%.

The reflectance measurement usually exhibits a baseline drift of up to 2% over the period of the measurement. Usually this drift is linear and by subtracting the baseline from the measurement the reflectance change can be determined with accuracy better than 0.02% [1,15]. It is interesting to compare the sensitivity of our apparatus to the sensitivity of the U4IR surface science equipment at the National Synchrotron Light Source (NSLS) - Brookhaven National Lab, where many broadband reflectance measurements have been performed [16-21]. Although the synchrotron provides radiation orders of magnitude

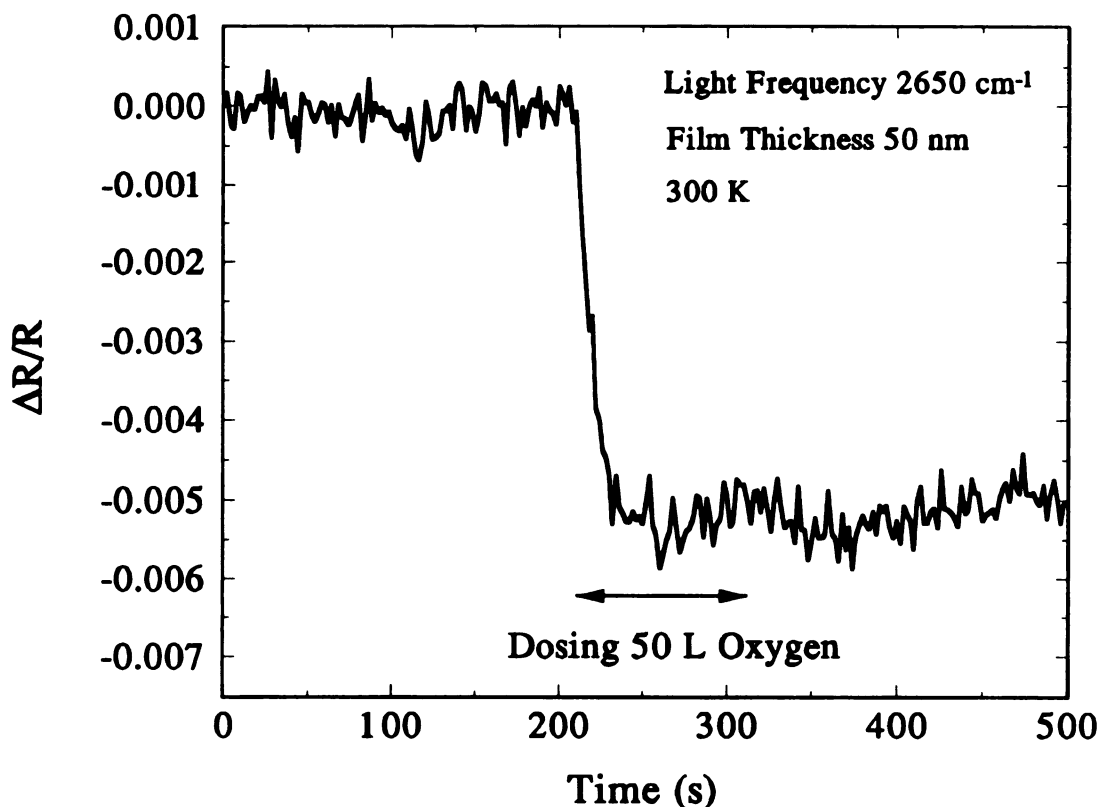


Figure 2-4. Broadband reflectance change $\Delta R/R$ of 50 nm thick Cu(100) film exposed to 50 Langmuirs (5×10^{-7} Torr for 100 seconds) of oxygen. The measurement is performed at room temperature. Total $\Delta R/R$ is about 0.5%.

brighter than the global, instabilities in the electron beam limit the sensitivity to broadband reflectance changes to 0.2% [18] - an order of magnitude worse than ours. A disadvantage of our system is that it can perform a measurement only at one particular IR frequency at a time, while the system at the U4IR beam line covers the whole frequency range $300 - 3000 \text{ cm}^{-1}$ at a time by using a Fourier Transform spectrometer (FTIR).

Combined resistivity and reflectance change measurements are further discussed in chapter 5.

References

- [1] C. Chung, Ph.D. thesis, Michigan State University, unpublished, (1993).
- [2] Multi-Scanning Systems Corporation, type RC-2.
- [3] R. G. Tobin, C. Chung and J.S. Luo, *J. Vac. Sci. Technol. A* **12** 264 (1994).
- [4] Milton Roy Co.
- [5] Cambridge Physical Sciences, IGP225.
- [6] Infrared Laboratories, Inc.
- [7] Thermionics.
- [8] Perkin-Elmer corp.
- [9] D. E. Kuhl and R. G. Tobin, *Rev. Sci. Instr.* **66**, 3016 (1995).
- [10] T. Takahagi, I. Nagai, I. Ishiytani, H. Kuroda and Y. Nagasawa, *J. Appl. Phys.* **64**, 3516 (1988).
- [11] T. Takahagi, I. Ishiytani, H. Kuroda, Y. Nagasawa, H. Ito and S. Wakao, *J. Appl. Phys.* **68**, 2187 (1990).
- [12] Y. J. Chabal, G. S. Higashi, K. Raghavachari and V. A. Burrows, *J. Vac. Sci. Technol. A* **7**, 2104 (1989).
- [13] P. Dumas, Y.J. Chabal and G. S. Higashi, *Phys. Rev. Lett.* **65**, 1124 (1990).
- [14] Princeton Applied research Corp.
- [15] D. E. Kuhl, Ph.D. Thesis, unpublished, (1996).
- [16] C. J. Hirschmugl, G. P. Williams, F. M. Hoffmann and Y. J. Chabal, *Phys. Rev. Lett.* **65**, 480 (1990).
- [17] C. J. Hirschmugl, G. P. Williams, F. M. Hoffmann and Y. J. Chabal, *J. Vac. Sci. and Technol. A* **12**, (1994).

[18] K. C. Lin, R. G. Tobin, P. Dumas, C. J. Hirschmugl and G. P. Williams, *Phys. rev. B* **48**, 2791 (1993).

[19] K. C. Lin, R. G. Tobin, P. Dumas, *Phys. Rev. B* **49** 17273 (1994).

[20] C. J. Hirschmugl, G. P. Williams, B. N. J. Persson and A. I. Volokitin, *Surf. Sci.* **317** L1141 (1994).

[21] C. L. A. Lamont, B. N. J. Persson and G. P. Williams, *Chem. Phys. Lett.* **243**, 429 (1995).

Chapter 3

Development of a Novel UHV Sample-Transfer and Sample-Handling System

3-1. Introduction

The fast sample introduction from air to ultra-high-vacuum (UHV) and sample transfer between different UHV chambers (evaporation, reaction, analysis), without breaking the vacuum, is vitally important for material and surface studies. The obtaining of a UHV usually takes about 72 hours or more, so breaking the vacuum for introducing a new specimen is very unproductive approach. Different groups and commercial manufacturers have developed a variety of fast entry *load-lock* systems complying with different requirements [1-16]. The usual method is to first introduce the sample into a small loading chamber, separated from the main UHV chamber by a gate valve. This loading chamber is easily and quickly (in about few minutes) pumped to a high vacuum (HV: low $10^{-6} - 10^{-8}$ Torr) pressure using pumps with high pumping speed. When the right pressure is achieved the gate valve to the main UHV chamber is opened and the sample is loaded in. The last step must be accomplished as fast as possible, so the pressure increase or spike in the main UHV chamber is as small as possible.

Different types of UHV transporters are used to move the sample in and out of the chamber and between different chambers: bellows sealed push-pull or air actuated,

bellows sealed rack and pinion, wobble stick manipulators and magnetically coupled rods. The last type [19], used in our design, provides adequate linear travel (up to 36 inches, for a 2.75" mounting flange), 360° rotational motion, and is relatively inexpensive. The operation is smooth and reproducible and the positioning is achieved by sliding an external sleeve, which is magnetically coupled to the transporter rod, on which a sample holder is attached. Applying too big an axial or rotational force leads to decoupling between the sleeve and the rod, thus preventing damage to the components of the sample securing and positioning system.

The general requirements for a sample transfer system include easy and reproducible transfer, heating and cooling range and method, electrical and thermocouple contacts to the sample and means of positioning inside the UHV chamber. Usually there is a variety of specific needs dictated by the particular experiment and configuration. The small diameter tubes of the UHV chamber, usually dedicated to the transfer system, and the limited techniques and materials complying with the UHV requirements of cleanliness (soldering, taping, gluing and materials like plastics and brass for instance are not allowed due to their high outgassing rate) make the design of a UHV transfer system a pretty challenging venture.

Our goal was to make simultaneous measurements of the dc electrical resistance and infrared reflectance of epitaxial copper films grown *in situ* on silicon substrates [17,18]. This application, together with the design of our preexisting chamber, imposed stringent requirements:

- 1) **Optical access to the sample surface at angles of 83 - 89° from the surface normal, so that there could be almost no projections above the surface plane that would shadow the surface.**

- 2.) **Total of *six* electrical contacts to be closed in the process of engaging to the sample holder inside the UHV chamber -- two for type K thermocouple and four for the resistivity measurement, thus permitting simultaneous and independent monitoring of the sample resistance and temperature.**

- 3.) **A sample size approximately 1 x 3 cm for maximum infrared signal.**

- 4.) **Fast, smooth and reliable transfer in and out of the UHV chamber. Precise and reproducible sample positioning for optical stability.**

- 5.) **Heating and cooling between 100 and 1000 K.**

- 6.) **Access through a 38 mm OD tube perpendicular to the manipulator axis.**

- 7.) **Sample electrically isolated from the sample mount.**

- 8.) **Good thermal contact between sample and sample mount to ensure effective cooling.**

9.) Thin film evaporation capability inside the UHV chamber.

Although different groups and commercial manufacturers have developed UHV transfer systems [1-16], none of them were able to successfully fulfill all of our requirements. The most critical one for our purposes, the need of six electrical contacts was not found in any of the existing designs. Similar geometries were available but providing no more than four electrical contacts. Thus in order to perform our combined resistivity-reflectance measurements I designed a novel UHV transfer system to comply with all of the nine requirements listed above.

3-2. General Operation of Our UHV Transfer System

The main components of our UHV transfer system are shown in Figure 3-1. Detailed sketches are shown in Figures 3-3 and 3-4. After preparation, the substrate is mounted on a disk-shaped carrier and introduced in the load-lock chamber using a special handling device. The load-lock chamber is a simple “six-cross” equipped with 2 viewports, ionization gauge tube for pressure monitoring, quick-access door and magnetically coupled transporter with a 3 prong fork. It is separated from the main UHV chamber by a metal sealed gate valve.

The carrier disk is engaged to the fork by first positioning the spring-loaded prongs inside 3 of the 6 key-shaped holes (2 on the top and 1 on the bottom of the carrier disk) and after that applying a clockwise rotation. After the quick-access door is closed, the

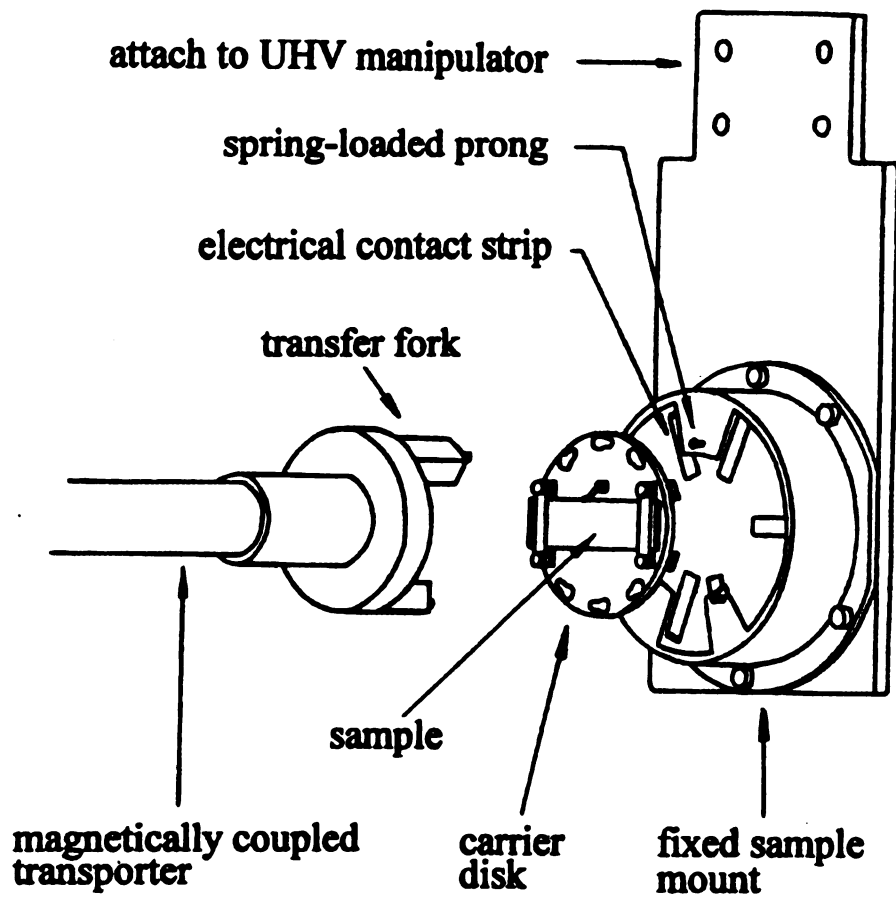


Figure 3-1. Main components of the UHV sample transfer system.

load-lock is pumped by a 90 l/s turbo pump mounted just below the chamber and backed by a mechanical pump. Pressure in the low 10^{-6} to mid- 10^{-7} Torr is achieved in a few minutes and the system is ready for the next step -- transfer of the carrier disk inside the main UHV chamber.

In order for the pressure spike in the main UHV chamber to be as small as possible the time interval when the gate valve separating it from the load-lock chamber is open should be minimized. This is achieved by careful alignment of the sample mount beforehand using the precision X-Y-Z manipulator mounted on a 360° rotatable mounting platform. When the sample mount is properly aligned, the gate valve is open and the carrier disk is advanced towards the sample mount using the magnetically coupled transporter, till the 3 spring-loaded prongs of the sample mount enter the 3 empty key-holes of the carrier disk. The disengagement from the fork and engagement to the sample mount is achieved simultaneously by counterclockwise rotation of the transfer rod. In the process of engaging the carrier disk to the sample mount 6 electrical contacts are closed -- 2 for the thermocouple and 4 for the resistivity measurement. Transferring of the carrier disk back to the manipulator fork follows the same procedure, just using opposite rotation of the transfer rod.

The concept utilizing 6 key-holes and spring-loaded prongs is based on a commercially available sample-transfer system by Thermionics NW. In their design the key shaped holes are evenly distributed around the perimeter of the carrier disk. In our design the key-shaped holes are clustered in two groups -- on the top and bottom of the carrier disk, this way allowing longer sample to be mounted on, which is strongly

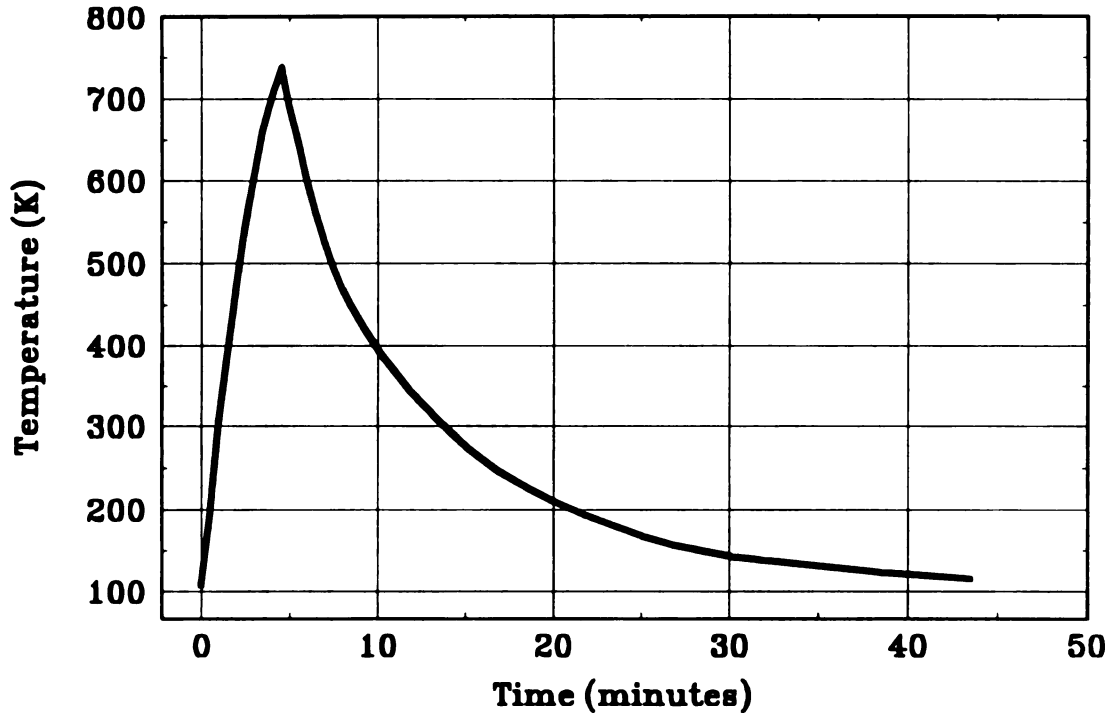
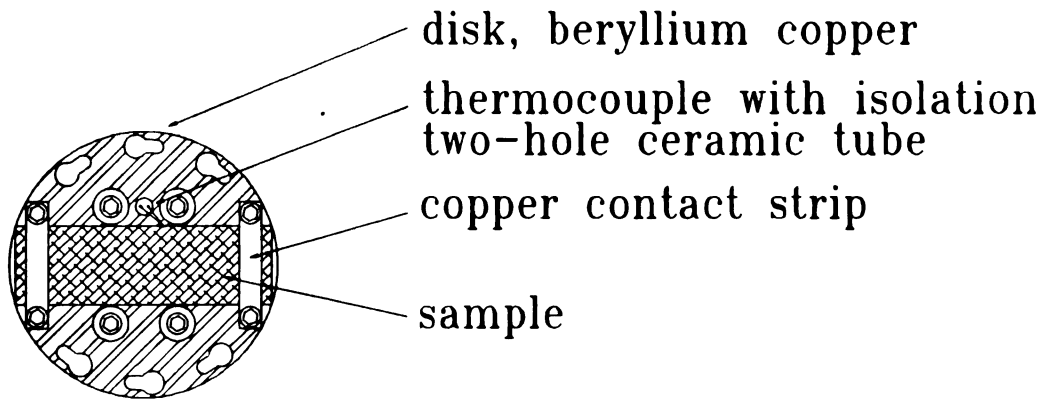


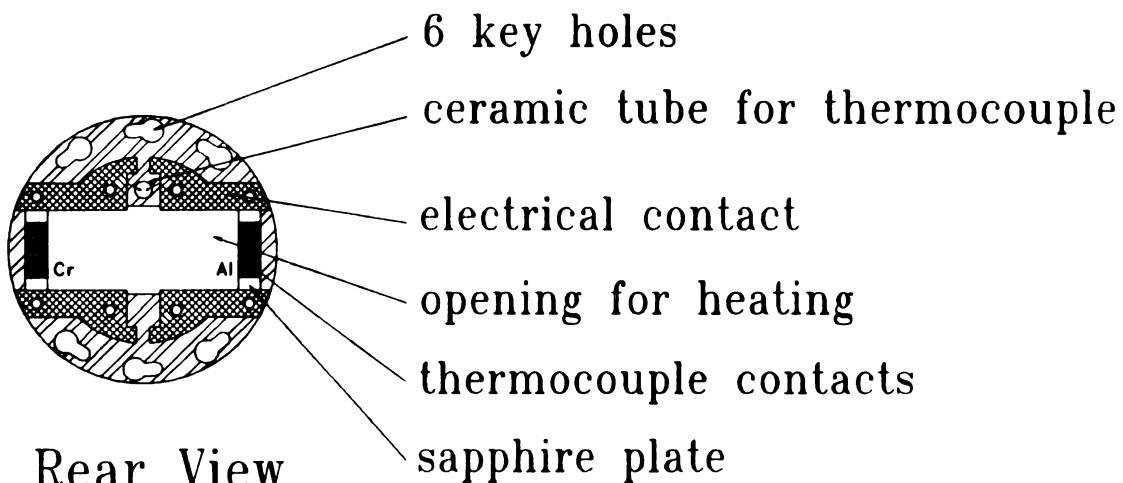
Figure 3-2. Starting at 105 K a copper sample is resistively heated up to 740 K, then cooled down to 115K.

beneficial for the reflectance measurement. Also the design by Thermionics did not provide 6 breakable electrical contacts to the sample, which is of crucial importance for our experiments.

The sample cooling is accomplished by attaching the sample mount to a liquid nitrogen (LN_2) reservoir or “cold finger”. The lowest temperature achieved is about 100 K. The sample is radiant heated by a nude tungsten filament. The temperatures of up to 1000K can be readily achieved. Figure 3-2 shows a heating/cooling curve for a copper sample. The sample was initially at temperature of 105 K. A filament current of 9.8 A



a) Front View



b) Rear View

Figure 3-3. Sample carrier disk.

heated it to 740 in about 5 minutes. The filament was then turned off. The sample reached 200 K in about 15 minutes, and 115 K in about 40 minutes. The cooling time constant is dominated by the thermal contact between the sample mounting disk and the tabs of the fixed sample mount; it could probably be further improved by coating these contact surfaces with silver or gold.

3-3. Carrier Disk

The carrier disk (Figure 3-3) is a very delicate device due to the variety of requirements it has to comply to and its tiny dimensions (32 mm OD and 1.6 mm thickness). It is made out of beryllium copper in order to provide good thermal contact with the sample mount for satisfactory sample cooling. At the same time the beryllium copper is a much harder material than the regular OFHC (oxygen free high conductivity) copper thus much less susceptible to wearing which is very important for reliable long-term operation. Besides the 6 key-shaped holes, clustered in 2 groups at the top and bottom of the disk, there is a large opening in the middle (23 x 10 mm) needed for the radiant sample heating by a nude tungsten filament on the sample mount. Also there are 8 holes for socket head screws and a hole for an isolation ceramic tube for the thermocouple.

Front view of the carrier disk, with sample attached, is shown in Figure 3-3a. The sample is held to the front of the carrier disk by a thin (0.13 mm) copper contact strip at each end. The strips make electrical contact to the sample, but are electrically isolated from the disk. These mounting strips are the only part of the assembly that projects

beyond the sample surface, and they are thin enough to produce negligible optical shadowing, even at near-grazing incidence. They are held in place by stainless steel 0-80 screws, which pass through alumina tubes to independent beryllium copper contact plates on the back side of the disk (Figure 3-3 b). Four additional screws, also electrically isolated from the disk, hold the contacts in place during assembly and prevent them from moving during installation and removal of the carrier.

The sample is electrically isolated from the disk by two crystalline sapphire plates (16 x 3.2 x 0.8 mm, with holes for the 0-80 screws), one at each end. In addition to providing electrical isolation, the sapphire plates have near-metallic thermal conductivity at liquid nitrogen temperature to facilitate cooling, but are good thermal insulators above room temperature, for efficient heating [20-24]. Two more sapphire plates separate the contact plates from the disk as shown in Figure 3-3b, and their center regions are wound with chromel and alumel thermocouple wire, respectively. The two thermocouple wires pass to the front of the disk through a short two-hole alumina tube and are joined to form a thermocouple junction. The thermocouple is pressed mechanically against the sample (for metal samples, it could be spot-welded). The four beryllium copper plates and the two sapphire plates wound with wire form the carrier side of the six electrical contacts. When the carrier is latched to the fixed mount, they press against the six spring contacts of the mount.

Four-wire resistance measurements generally require four independent electrical contacts to the sample. In our design the two contacts at each end of the sample are both made through the thin copper strip that holds the sample to the carrier disk, so any contact

resistance between the strips and the sample is included in the measured resistance. We have found this contribution to be $<0.01 \Omega$, which is negligible for our purposes (typical sample resistance is 2 to 3 Ω). The resistance between the fixed spring contacts and the carrier can be as large as 1 Ω , but does not contribute to the measured resistance. A true four-wire carrier could be constructed with only a slight increase in complexity, eliminating from the measurement the small resistance between the contact strips and the sample.

Once assembled the carrier disk is sturdy and tolerates several feet drops without damage. Another very useful feature is that the sample mounting procedure is fast -- in about 2 - 3 minutes the sample is secured in place and the disk is ready for transfer. This is very important for hydrofluoric acid (HF) etched silicon samples, when the exposure to the ambient atmosphere needs to be as short as possible.

3-4. UHV Sample Mount

The UHV sample mount (sample holder) hosts the carrier disk inside the main UHV chamber. It is attached to a liquid nitrogen reservoir (cold finger) using an OFHC copper clamp. The cold finger is mounted on an X-Y-Z- θ manipulator, allowing precise positioning. Feedthroughs are provided for 2 thermocouples, 4 electrical wires for resistivity measurement and 2 high current heater leads.

The main body of the sample mount consists of 2 parts, head (SMH) and plate (SMP), which are held together by 6 socket-head screws (Figure 3-4). The head is made out of beryllium copper and accommodates the electrical contacts and prong-locking

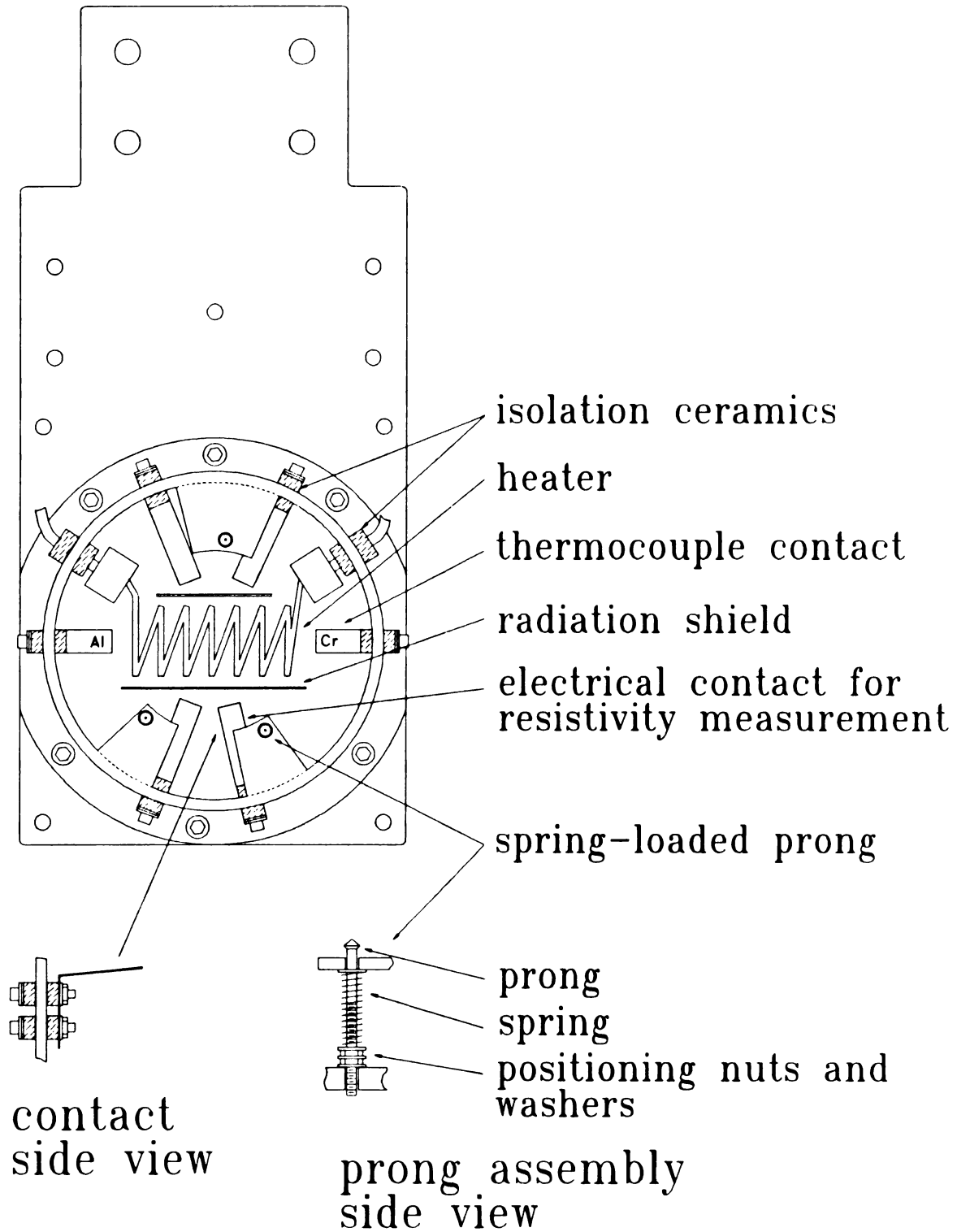


Figure 3-4. UHV sample mount.

mechanism. The plate, made out of OFHC copper, provides connection to the cold finger, holds the sample heater and has a number of threaded holes for attaching shields, isolation ceramics and a thermocouple. It also plays a role in the operation of the spring-loaded prong-locking mechanism.

Six Γ -shaped electrical contacts are distributed around the sample mount head. They are attached to the SMH using 0-80 stainless steel socket head screws and electrically isolated via alumina tubes and washers (see contact side view in Figure 3-4). As it was very difficult to obtain chromel and alumel sheet material for the thermocouple contacts the following approach was used. Commercially available 0.8 mm (0.032") chromel and alumel wire was flatten out by hammering to form a sheet about 3 mm wide and 0.2 mm thick. The contacts made this way proved to have excellent springiness and made very reliable and reproducible electrical connection with the corresponding contacts on the sample ring (less than 1 Ω contact resistance). Another advantageous property was that they completely preserved their springiness while exposed to very wide temperature range - cooling down to about 100 K and heating at least up to 1000K as they are very closely positioned to the sample heater. A wire of the corresponding thermocouple material was spot-welded to each of the contacts and via an alumina tube conveyed out of the SMH. Using a thermocouple feedthrough guaranteed that each half of the thermocouple from the sample to the outside of the UHV chamber is composed of alumel or chromel, thus avoiding unwanted junctions with other materials. Due to the good performance of the "home-made" sheet material the 4 electrical contacts for the resistivity measurement were made also out of chromel.

The mechanism for securing the carrier disk into place on the sample mount incorporates 3 spring-loaded prongs (Figure 3-4). They are positioned on the 3 fingers of the SMH, designed to provide maximum thermal contact with the carrier disk. As the carrier disk thickness is 1.6 mm the prong's head should be elevated above the plane of the SMH fingers. This is achieved by using positioning nuts and washers, pressing on the sample mount plate (see prong assembly side view in Figure 3-4).

The sample heating is radiant, provided by a nude tungsten filament attached to the sample mount plate, and electrically isolated using ceramics. The heater is embraced by a copper shield concentrating the heat to the sample and protecting the stainless steel springs of the prongs from losing their springiness and collapsing. Since both the filament and the sample are electrically isolated from ground, it would be straightforward to implement electron-beam heating.

3-5. Concluding Remarks

In this chapter I presented the development of a *novel* UHV sample transfer system, providing *6 breakable contacts* between the sample and the UHV sample holder, optical access to the sample at grazing angles of incidence, capability of transferring large samples, wide temperature range (110 - 900 K) and easy and reliable operation. None of the commercially available transfer systems were able to comply to the requirements for number of contacts and sample size together with the 2.75" flange size limitation imposed by our configuration. For about one and a half years of reliable operation our transfer system proved to be perfectly adequate for our needs. It was also successfully used for

some experiments performed in the surface science UHV chamber at the U4IR far-infrared beam line at the National Light Source at Brookhaven National Laboratory showing its portability and adaptability to different configurations. We submitted a paper describing our sample-transfer and sample-handling system to the Journal of Vacuum Science and Technology.

References

- [1] C.A. Crider, G. Cisneros, P. Mark and J.D. Levine, *J. Vac. Sci. Technol.* **13**, 1202 (1976).
- [2] J.P. Hobson and E.V. Kornelson, *J. Vac. Sci. Technol.* **16**, 701 (1979).
- [3] B.J. Mulder, *J. Phys. E* **12**, 908 (1979).
- [4] N.J. DiNardo, J.E. Demuth, W.A. Thompson and P.G. Ledermann, *Rev. Sci. Instr.* **55**, 1492 (1984).
- [5] J. Klebanoff, V.H. Ritz and R.E. Thomas, *J. Vac. Sci. Technol. A* **2**, 1396 (1984).
- [6] K.W. Nebesny and N.R. Armstrong, *J. Vac. Sci. Technol. A* **3**, 1763 (1985).
- [7] J.M. Lindquist and J.C. Hemminger, *J. Vac. Sci. Technol. A* **5**, 116 (1987).
- [8] G.S. Chottiner, W.D. Jennings and K.I. Pandya, *J. Vac. Sci. Technol. A* **5**, 2970 (1987).
- [9] A.Z. Moshfegh and A. Ignatiev, *Rev. Sci. Instrum.* **59**, 2202 (1988).
- [10] H.-J. Drouhin, M. Picard and D. Paget, *Rev. Sci. Instr.* **60**, 1167 (1989).
- [11] R.E. Clausing, L. Heatherly and L.C. Emerson, *J. Vac. Sci. Technol.* **16**, 708 (1979).
- [12] R.S. Polizzotti and J.A. Schwarz, *J. Vac. Sci. Technol.* **17**, 655 (1980).
- [13] A.L. Helms, Jr., W.A. Schiedt and S.L. Bernasek, *Rev. Sci. Instr.* **59**, 1223 (1988).
- [14] R. Raval, M.A. Harrison, D.A. King and G. Caine, *J. Vac. Sci. Technol. A* **9**, 345 (1991).
- [15] X.-S. Wang, C. Huang, V. Bressler-Hill, R. Maboudian and W.H. Weinberg, *J. Vac. Sci. Technol. A* **11**, 2860 (1993).
- [16] S. Thevuthasan, D.R. Baer, M.H. Engelhard, Y. Liang, J.N. Worthington, T.R. Howard, J.R. Munn and K.S. Rounds, *J. Vac. Sci. Technol. B* **13**, 1900 (1995).
- [17] E.T. Krastev, L.D. Voice and R.G. Tobin, *J. Appl. Phys.* **79**, 6865 (1996).
- [18] E.T. Krastev, D.E. Kuhl and R.G. Tobin, *Surf. Sci. Lett.*, *in press*.

- [19] Model MT-16, MDC Vacuum Products, 23842 Cabot Blvd., Hayward, CA 94545.
- [20] R.W. Powell, C.Y. Ho and P.E. Liley, ed., *Thermal Conductivity of Selected Materials* (National Bureau of Standards, 1966).
- [21] W.E. O'Grady, A.V. Melo, R.W. Hoffman and G.S. Chottiner, *J. Vac. Sci. Technol. A* **5**, 281 (1987).
- [22] J.D. Beckerle, Q.Y. Yang, A.D. Johnson and S.T. Ceyer, *Surf. Sci.* **195**, 77 (1988).
- [23] P.G. Strupp and P.C. Stair, *J. Vac. Sci. Technol. A* **9**, 2410 (1991).
- [24] C. Rusu and J.T. Yates, Jr., *J. Vac. Sci. Technol. A* **15**, 436 (1997).

Chapter 4

Surface Morphology and Electrical Conductivity of Epitaxial Cu(100) Films Grown on H-Terminated Si(100)

4-1. Introduction

This chapter is based on our paper published in Journal of Applied Physics [1].

Hydrogen-terminated silicon surfaces prepared by wet chemical etching have been shown to be excellent substrates for growing epitaxial films of a variety of fcc and bcc metals [2-9]. In most cases a thin layer of epitaxial copper is used as a seed layer for subsequent growth of other metals. For this reason, and because the low electrical resistivity and large electromigration resistance of copper make it an important technological material, [10] the properties of epitaxial copper films on Si are of particular interest. We report here an investigation of the crystal structure, surface morphology and electrical conductivity of such films as a function of deposition rate, deposition temperature and post-deposition annealing. Epitaxial growth is observed over a wide range of deposition conditions. The smoothest films were obtained by near-room-temperature growth at rates of 0.1-1.0 nm/s; higher temperatures and higher deposition rates produced noticeably inferior films. Post-deposition annealing at temperatures up to 125°C had little effect, while higher temperatures degraded the films.

There have been a number of studies of epitaxial Cu films grown on H-terminated Si, [10-14] but important aspects, including their surface roughness and the nature of the Si-Cu interface, are not yet understood. It has been reported that the films, although epitaxial, are not atomically smooth [14]. There has been no previous systematic investigation of the surface morphology, however, or of the influence of deposition conditions and post-deposition treatment on the morphology. The present work presents such an investigation, together with new information on aspects of film composition and structure that affect electrical transport.

An earlier study [14] revealed the existence of a mixed "buffer layer" about 10 nm thick between the Si and the Cu, which is presumably important in facilitating epitaxy. Reflection high-energy electron diffraction (RHEED) [14] and grazing incidence X-ray diffraction [13] studies have shown that the Cu lattice is rotated by 45° relative to the Si lattice, with Cu(010) parallel to Si(011). The rotation reduces the lattice mismatch between the two materials from 40% to 6%. Even a 6% mismatch, however, is unusually large for epitaxial growth. The buffer layer presumably helps to relieve the strain, but its nature — for example, whether it is compositionally disordered or a stoichiometric silicide — has not been established. Our work confirms many of these conclusions, and demonstrates that the buffer layer, though it may contain Si as an impurity, is not a stoichiometric silicide, but is structurally indistinguishable from pure Cu.

Measurements of electrical resistance as a function of thickness during deposition provide additional clues to the quality and composition of the films. The first few nm of the film consist of discontinuous Cu grains. The remainder of the film is relatively pure Cu

(defect density of a few tenths percent) but with a high level of surface, interface or grain boundary scattering that strongly affects film conductance at thicknesses below about 50 nm.

4-2. Film structure and surface morphology

The copper films were deposited in a resistive evaporator with base pressure 1×10^{-8} Torr. The (100) Si substrates (B-doped, 20-50 Ω cm resistivity) were prepared by ultrasonic degreasing with acetone and methanol, etching for 30 - 60 seconds in a 10% aqueous solution of HF, and pull-drying (slowly and smoothly removing the substrate from the solution with the surface vertical, so that the liquid sheets off smoothly with no droplets). It has been shown that such a procedure leads to an extremely flat and chemically inert surface, with virtually all the Si dangling bonds terminated with H [15-18]. After etching, the samples were loaded into the evaporator and pumping was begun as quickly as possible — within less than five minutes. A pressure of the order of 5×10^{-8} Torr was achieved in about 15 minutes. The substrates were clamped to a variable-temperature stage so that effects of elevated substrate temperature and post-deposition annealing could be studied. The temperature was measured by a type K thermocouple mounted on the heating stage, close to the sample. The substrate was not intentionally heated, but the thermocouple on the evaporation stage typically indicated a temperature of 25-30°C during deposition. The evaporation rate and film thickness were measured using a quartz crystal monitor calibrated with a diamond stylus profilometer. Most of the films had thicknesses of about 100 nm. During deposition the pressure rose to between 5×10^{-8}

and 3×10^{-7} Torr. This is an unusually high pressure for epitaxial growth, and results in a significant impurity concentration in the film, as we discuss below. It is a remarkable feature of the H-terminated Si surface that oriented Cu films can be grown even at pressures of 10^{-4} Torr [19].

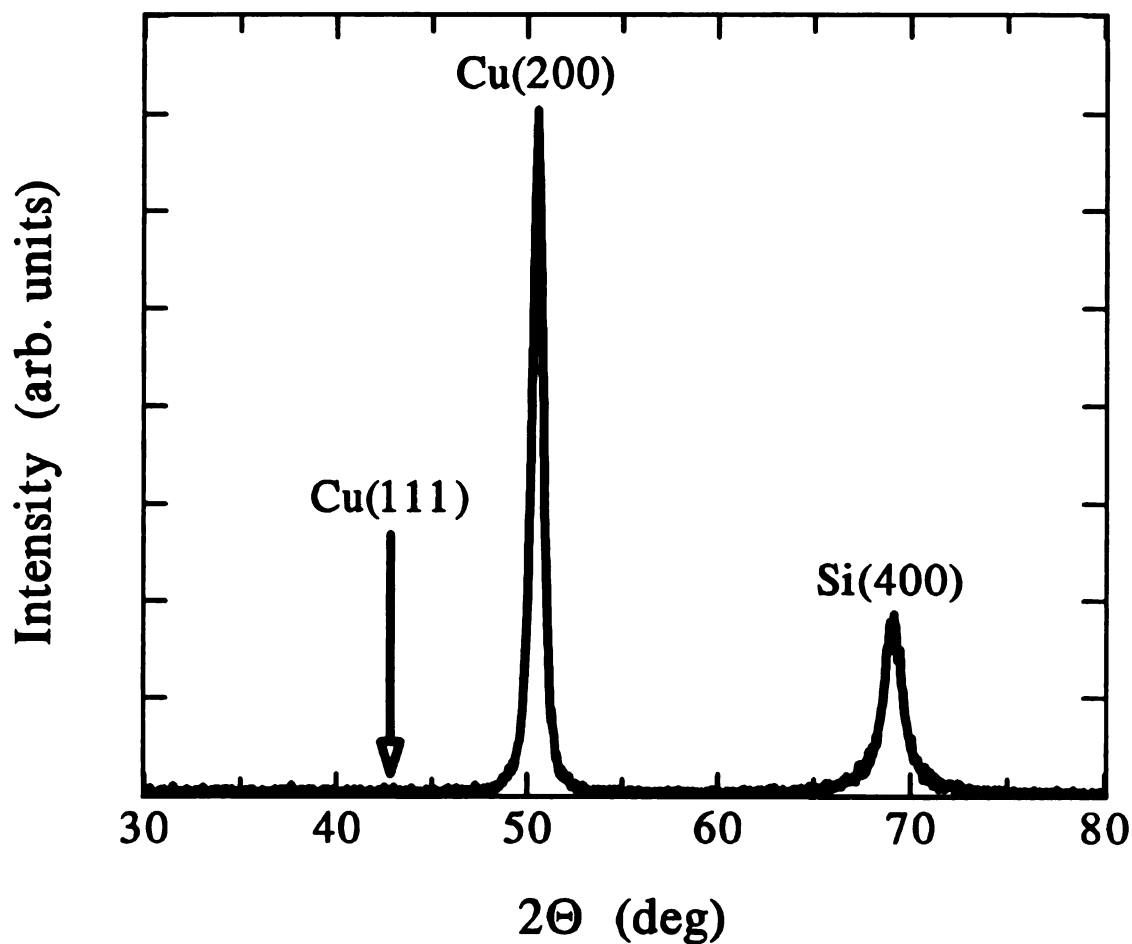


Figure 4-1. θ - 2θ X-ray diffraction pattern of 100 nm thick Cu film deposited on H-terminated Si(100) at 0.1-0.2 nm/s evaporation rate, without intentional heating. The strong Cu(200) peak and absence of a Cu(111) peak indicate highly oriented growth.

The crystal structure of the films was determined using X-ray diffraction (XRD). The orientation in the direction perpendicular to the surface was characterized by standard θ - 2θ scans using Cu $K\alpha$ radiation. Completely disordered (powdered) Cu exhibits a (111) peak 2.17 times more intense than the (200) peak [20]. Polycrystalline Cu films grown on glass, alumina, or oxidized Si substrates typically show a *larger* (111):(200) ratio, indicating preferential (111) orientation, [13,20] but both peaks are much weaker than the Si(400) peak since only a small fraction of the film volume contributes to each Cu peak. A typical scan of a film grown on an *etched* (H-terminated) Si(100) substrate is shown in Figure 4-1. Highly-oriented growth in the direction perpendicular to the surface, with the Cu[100] direction aligned with Si[100], is signaled by a Cu(200) peak at least as strong as the Si(400) peak, and *no* detectable Cu(111) peak.

The in-plane orientation of our films was determined by means of X-ray pole figures [21,22]. The source-detector angle was set to the Bragg angle for diffraction from Cu(111) planes, and the sample angle was varied over the full range of radial (Θ) and azimuthal (Ψ) angles using a four-circle goniometer. Figure 4-2 shows a Cu(111) pole figure [21] of a 100 nm thick copper film. The radial angle Θ is the angle between the film normal and the plane of incidence; the azimuthal angle Ψ represents rotation about the surface normal. A completely disordered film would produce a uniform intensity, independent of either angle. A (100) film that was disordered in the plane would exhibit a ring at $\Theta = 55^\circ$. The four pronounced Cu(111) poles in Figure 4-2 demonstrate that our samples are fully epitaxial. By comparing the integrated intensity in the poles with the background intensity we estimate that >95% of the sample volume is epitaxial. The width

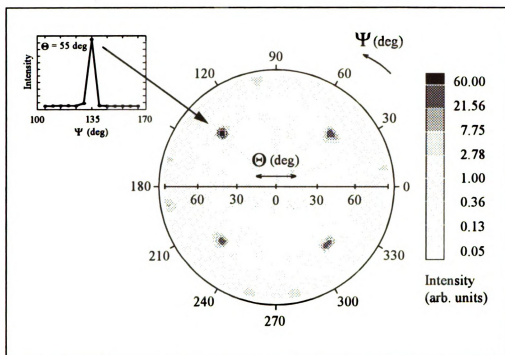


Figure 4-2. Cu(111) X-ray pole figure of a 100 nm copper film grown on H-terminated Si(100). Equal areas in the figure represent equal solid angles. The four sharp poles at $\Theta = 55^\circ$ demonstrate that the Cu film is epitaxial. The inset shows a scan through one of the poles in the azimuthal (Ψ) direction keeping the radial angle constant ($\Theta=55^\circ$). The width of the pole is instrument-limited.

of the poles in the azimuthal direction, shown in the inset, is limited by the instrumental resolution. A Si(111) pole figure of the Si substrate was very similar in appearance, except that the four poles were rotated by 45° in Ψ , in agreement with earlier reports that the copper lattice is rotated 45° with respect to the silicon lattice [13,14].

The surface morphology was studied in air using a commercial atomic force microscope [23] (AFM) with nominal 0.1 nm vertical resolution and 2-5 nm lateral resolution. Most of our scans represent a $1 \times 1 \mu\text{m}^2$ area of the surface. The raw

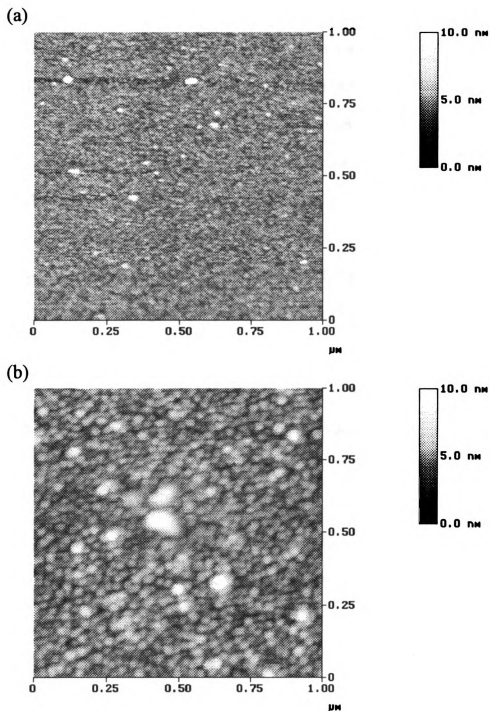


Figure 4-3. AFM topographical images of area $1 \times 1 \mu\text{m}^2$ for two different film thicknesses -- a) 7.5 nm and b) 100 nm. The z-range for both images is 10 nm and the RMS roughness is 0.71 nm for (a) and 0.95 nm for (b). Both films were grown near room temperature and were not annealed.

topographical images were software processed to eliminate the image bow in the y direction, spurious horizontal stripes, and tilt in the x axis. The primary measure of surface roughness used was the root-mean-square (RMS) deviation of the height from the mean. Scans of bare Si substrates yielded RMS roughness values of 0.2 - 0.3 nm.

Figure 4-3 shows typical AFM images for samples of 7.5 nm and 100 nm thickness. The deposition rate for both samples was 0.1-0.2 nm/s and the substrate was not intentionally heated. The brightness represents surface height, with brighter areas higher than darker ones, and both images use the same vertical and horizontal scales. Both films exhibit a granular structure, with individual grains 5-10 nm in diameter — comparable to the film thickness — for the 7.5 nm thick film and 2-3 times larger for the 100 nm film, with a few very large (50 nm) grains. The RMS roughness of the thinner film is 0.71 nm versus 0.95 nm for the 100 nm film. Clearly the films, although epitaxial, are rough on the atomic scale. These measurements confirm and quantify the conclusion of Demczyk *et al.*, [14] based on RHEED patterns, that the film growth is three-dimensional. On a larger length scale, however, the 100 nm film is relatively smooth, varying in height by a few nm over a lateral distance of tens or hundreds of nm.

X-ray diffraction from the 7.5 nm thick film revealed only a distinct Cu(200) peak, as in Figure 4-1; there was no evidence of copper silicide peaks. At this thickness the film consists of grains of crystalline copper which are still not fully connected. If there is intermixing of the Cu and Si as reported by Demczyk *et al.*, [14] it does not affect the crystalline structure.

We investigated the effect of varying the deposition rate from 0.1 to 3.5 nm/s, without intentional heating of the substrate. All of the films showed good adhesion to the substrate and appeared mirror-like with the characteristic red color of Cu. X-ray analysis showed strongly oriented growth for deposition rates up to 2 nm/s, but films deposited at 3.0 - 3.5 nm/s exhibited a Cu(111) peak comparable in intensity to the (200) peak, indicating polycrystalline structure. All of the epitaxial films showed surface morphologies similar to that of Figure 4-3b, and the roughness depended only very weakly on deposition rate. Figure 4-4 shows RMS roughness as a function of deposition rate. For rates up to 1 nm/s the RMS roughness is 0.5 - 2.0 nm; at higher deposition rates the roughness increases to as much as 4 nm.

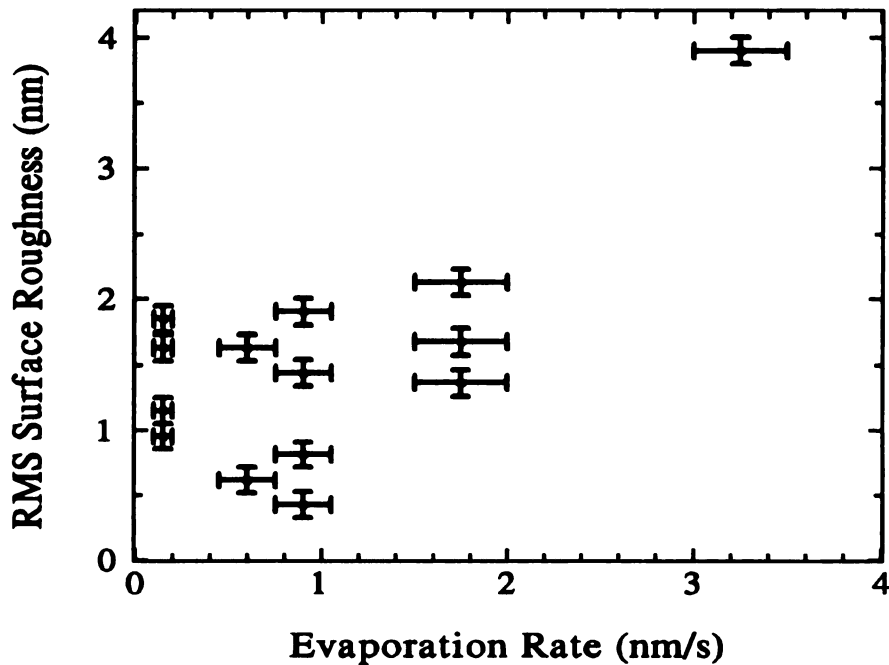


Figure 4-4. RMS roughness vs. deposition rate for 100 nm thick films grown without intentional heating of the substrate. Each data point represents a $1 \times 1 \mu\text{m}^2$ area of a different sample.

It is apparent from Figure 4-4 that films grown under nominally identical conditions can exhibit significantly different surface roughness. Figure 4-5 shows an AFM micrograph of a film grown under conditions nominally identical to those used for Figure 4-3b. The lateral scale is the same as in Figure 4-3, but the vertical range is twice as great, since the RMS roughness of the film in Figure 4-5 is 1.82 nm, nearly double that of Figure 4-3b. Much greater coalescence of the crystallites has taken place, leading to larger grains and deeper holes.

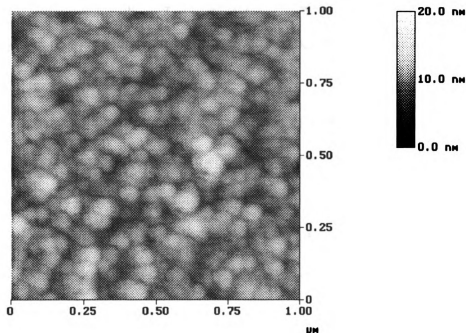


Figure 4-5. AFM topographic image of area $1 \times 1 \mu\text{m}^2$ of a 100 nm Cu film grown under conditions nominally identical to those for the film shown in Fig. 3b. The z-range is 20 nm, and the RMS roughness is 1.8 nm. Note the much larger grains and deeper holes.

These variations are perhaps not surprising in view of the high background pressure during deposition. We believe that they arise from uncontrolled variations in the experimental procedure, such as pull-drying technique, time in air before pumpdown, background pressure during deposition, atmospheric humidity, or variations in deposition rate. In the case of Figures 4-5 and 4-3b, we suspect that the differences are related to atmospheric humidity, which was much higher for the film shown in Figure 4-5 than for those shown in Figure 4-3. The bulk crystal structure, as revealed by XRD, was insensitive to such variations.

Intentionally heating the substrate during deposition, to temperatures between 100°C and 250°C, resulted in extremely poor films. The films had a dark brown color, and XRD scans showed no peaks attributable to Cu, but a variety of weak peaks similar to those observed by Chang, [12] and attributed to a mixture of Cu_3Si and Cu_4Si . These results agree with the observation of Demczyk *et al.* that substrate temperatures above (or below) room temperature produce inferior films [14].

We also investigated the effect of post-deposition annealing in vacuum, for films grown near room temperature at deposition rates of 0.1 - 0.2 nm/s. The results are summarized in Table 4-1. Following deposition the stage was heated to an annealing temperature (125, 150, 175 or 200°C) over a period of about 15 minutes. The stage would then be held at the annealing temperature for 15 minutes and allowed to cool in vacuum for about eight hours before the sample was removed from the evaporator for characterization.

Table 4-1. Characteristics of 100 nm copper films annealed in vacuum at different temperatures. All of the films were deposited at rates of 0.1 - 0.2 nm/s, with no intentional heating of the substrate during deposition.

Annealing Temperature	Visual Appearance	Crystal Structure	Surface Morphology	RMS Roughness
not annealed	reddish metal shine, mirror like	epitaxial Cu	grains	1-2 nm
125°C	reddish metal shine, mirror like	epitaxial Cu	grains	1-2 nm
150°C	reddish, cloudy	epitaxial Cu	clusters and holes	2 nm
175°C	reddish, cloudy	epitaxial Cu	channels	8 nm
200°C	dull gray-brown	Cu ₃ Si	not studied	not studied

Epitaxial structure was preserved for annealing temperatures up to 175°C. Films annealed at 125°C were essentially indistinguishable from unannealed films in surface morphology and roughness. A film annealed at 150°C exhibited the same RMS roughness as an unannealed film, but the AFM images showed the formation of larger copper grains and the appearance of deep holes in the surface. Visually the surface appeared cloudy, as though covered by a whitish haze. These features became more pronounced for films annealed at 175°C, as shown in Figure 4-6. The holes became larger and deeper, extending almost to the surface of the Si (50-60 nm) and forming channel-like structures around the enlarged copper clusters. The RMS roughness increased to 8 nm for an annealing temperature of 175°C.

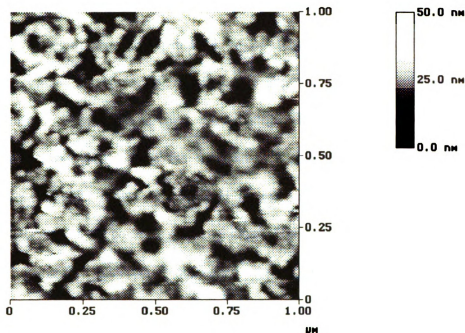


Figure 4-6. AFM topographical image of a 100 nm Cu film annealed in vacuum at 175°C after deposition near room temperature. The z-range is 61 nm. The channels penetrate deep into the film, nearly to the Si surface.

The picture changed dramatically for the films annealed at 200°C. Immediately after removal from the evaporator they appeared shiny but gray, and XRD performed within a few hours after removal from vacuum showed only a distinct peak attributable to the (320) planes of Cu_3Si , indicating that the film had reacted completely with the Si. This is in agreement with the Chang's observation that the (100) Cu films react rapidly with Si at 200°C [12]. After the samples annealed at 200°C were kept in air for one day the color changed to dull gray-brown and instead of the pronounced (320) Cu_3Si peak a large number of small peaks was detected by XRD. This behavior is consistent with rapid oxidation of the copper silicide at room temperature.

4-3. Electrical conductivity

A significant amount of work on the electrical properties of our films was done by Larry Voice. Four-wire DC resistance measurements were made of selected films during deposition. For these samples contact strips (150 nm Ag on top of 10 nm Cr) were deposited on each end of the substrate. The substrate was then removed from the evaporator and etched as described in section II. Some pitting of the silver was observable, but the contacts remained intact. The sample was mounted on the evaporation stage using four phosphor-bronze clips pressing on the contacts, with separate electrical connections for the current and voltage leads. Cu was then deposited at a rate of 0.1 - 0.4 nm/s to a thickness of 100-400 nm using the procedures described above. The resistance of the film was continuously monitored as a function of film thickness t during the deposition.

Figure 4-7 shows the apparent film resistivity $\rho(t)$ as a function of t for a typical sample. The resistivity drops rapidly with increasing thickness. The very large range of ρ values, strong variation with t , uncertainty in the absolute thickness, and non-negligible parallel resistance due to the substrate make it difficult to analyze the data in this form. A more tractable quantity is the conductance derivative $dG(t)/dt$, where $G(t)$ is the conductance of the film at thickness t . This quantity is plotted in Figure 4-8 for the same film. It is apparent in Figure 4-8, for example, but not in Figure 4-7, that little change in conductance occurs for about the first 5 nm. Our use of the conductance derivative is similar to the approach of Fischer, Hoffmann and Vancea in their study of rough platinum films [24].

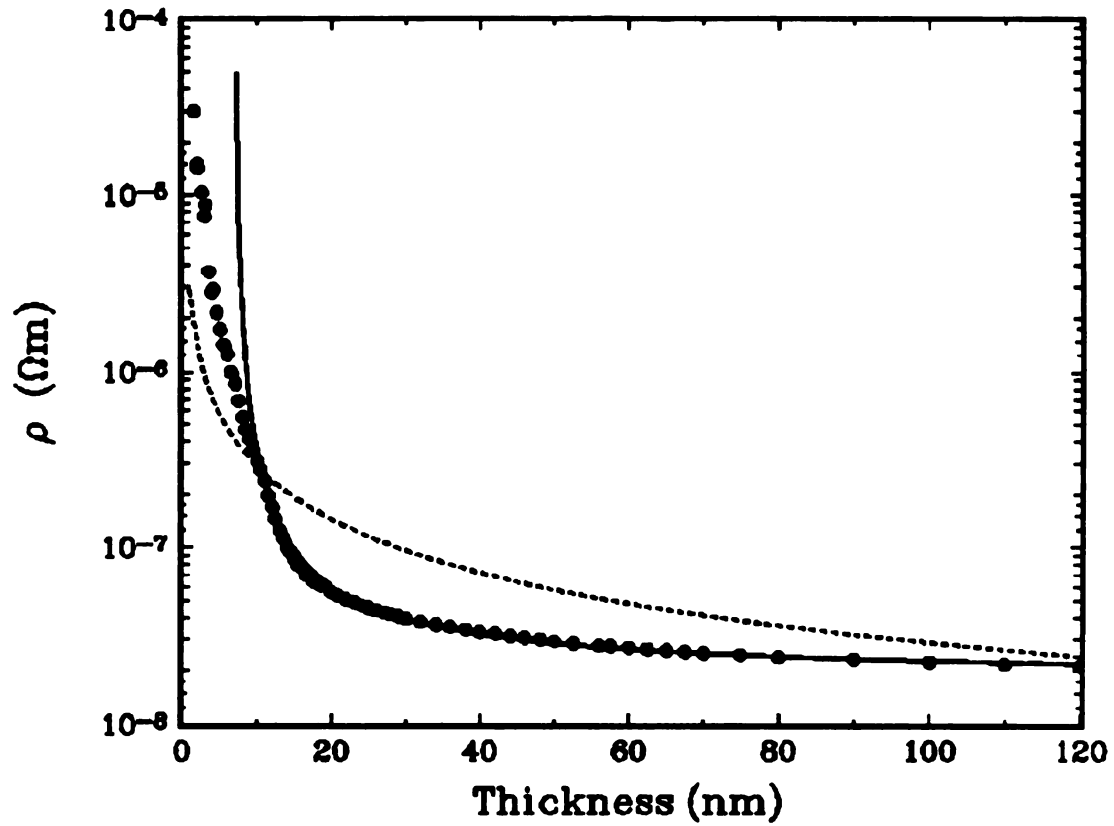


Figure 4-7. Apparent resistivity of a Cu film of thickness $t = 120$ nm grown near room temperature at approximately 0.1 nm/s. The dashed line is the best fit to the Fuchs-Sondheimer theory, Eq. 4-2. The solid line assumes an initial insulating layer of thickness t_0 , Eq. 4-5. The fitting parameters are given in the text.

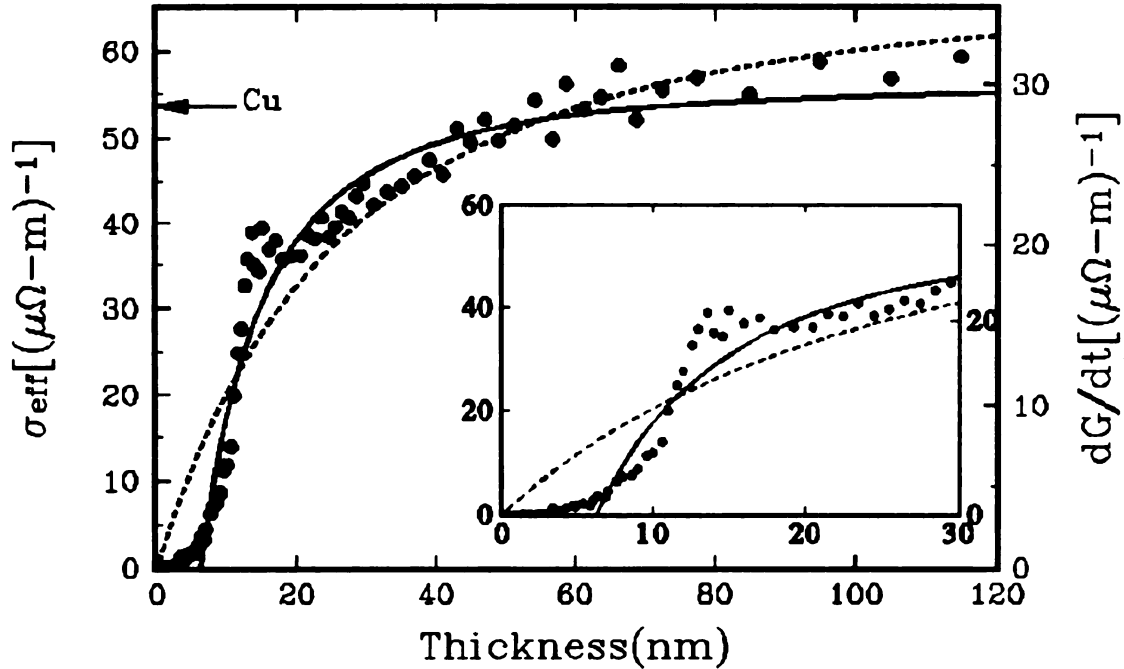


Figure 4-8. Effective conductivity $\sigma_{eff}(t)$ (defined by Eq. 1) of the same Cu film as in Fig. 7. The dashed line is the best fit to the Fuchs-Sondheimer theory, Eq. 4-4. The solid line assumes an initial insulating layer of thickness t_0 , Eq. 4-5. The fitting parameters are given in the text. The inset shows the 0 - 30 nm region on an expanded scale. The arrow indicates the conductivity of pure Cu at the deposition temperature.

To remove geometrical factors we define an effective conductivity:

$$\sigma_{eff}(t) = \frac{L}{W} \frac{dG(t)}{dt} \quad (4-1)$$

where W and L are the width and length of the film, respectively. In the limit that the thickness is much greater than the electronic mean free path, σ_{eff} can be interpreted as the bulk conductivity of the layer of material at thickness t . For uniform material σ_{eff} should approach the bulk conductivity at large thicknesses, as it does in Figure 4-8.

At smaller thicknesses, diffuse scattering of conduction electrons from surface defects and grain boundaries reduces σ_{eff} . The effects of surface scattering are often described within the Fuchs-Sondheimer model of the classical size effect, [24-32] which gives an expression for the effective resistivity of a thin film:

$$\rho(t) = \rho_0 \left[1 + \frac{\tilde{\ell}}{t} \right] \quad (4-2)$$

where ρ_0 is the bulk resistivity of the material, and

$$\tilde{\ell} = \frac{3}{8} \left(1 - \frac{p_v + p_s}{2} \right) \ell_0 \quad (4-3)$$

is an effective mean-free-path, with p_v and p_s the phenomenological specular scattering probabilities at the film-vacuum and film-substrate interfaces respectively and ℓ_0 the bulk electron mean free path. Although strictly valid only for $t \gg \ell_0$, Equation (4-2) has been shown to be a good approximation for $t/\ell_0 > 0.1$ [29-32]. For copper at room temperature $\ell_0 \approx 39$ nm. If the intrinsic conductivity of the deposited material is uniform, the effective conductivity defined by Equation 4-1 will have the form:

$$\sigma_{eff}(t) = \sigma_0 \left[1 - \frac{\tilde{\ell}^2}{(t + \tilde{\ell})^2} \right] \quad (4-4)$$

where σ_0 is the bulk conductivity. Equations 4-2 to 4-4 assume plane parallel interfaces, uniform film composition and structure, and thickness-invariant surface scattering. Significant deviations from Equation 4-4 would imply that one or more of these assumptions is violated.

The dashed curve in Figure 4-8 shows the best fit to Equation 4-4, and clearly fails to reproduce the data. Instead of increasing sharply at low t , the data are nearly flat up to about 6 nm. This indicates that the film's resistance does not initially decrease as rapidly as we would expect for a uniform continuous film of copper. Our XRD data for films less than 10 nm thick clearly show that the film consists of crystalline copper and not, for example, a high-resistance silicide. The most likely explanation, consistent with the AFM images, is that at thicknesses less than about 6 nm the film is discontinuous. Similar results were observed for Pt films by Fischer *et al.* [24]. In our measurements some decrease in resistance occurs even at low thicknesses because the presence of the Cu grains decreases the apparent resistance of the Si substrate.

Our goal is to determine whether the basic form of the $\sigma_{eff}(t)$ curve can be explained by surface scattering, and to estimate the specularity parameter p . Since the detailed form of the curve is rather complex and varied from run to run, we have not attempted a detailed analysis in terms of a roughness parameter, such as was used in Ref. 24. As a first approximation, we model the first few nm of the film as an insulating layer of thickness t_0 . Subsequent growth of uniform material will then give an effective conductance curve of the form:

$$\sigma_{eff}(t) = \sigma_0 \left[1 - \frac{\tilde{\ell}^2}{(t - t_0 + \tilde{\ell})^2} \right] \quad t \geq t_0 \quad (4-5)$$

The solid line in Figure 4-8 shows the best fit of Equation 4-5 to the data for $t > 8$ nm.

The best-fit parameters for this film were:

$$\begin{aligned}\sigma_0 &= 55 \begin{matrix} +5 \\ -2 \end{matrix} (\mu\Omega \text{ m})^{-1} \\ \tilde{\ell} &= 15 \begin{matrix} +5 \\ -2 \end{matrix} \text{ nm} \\ t_0 &= 7.0 \begin{matrix} +0.5 \\ -1.4 \end{matrix} \text{ nm} \end{aligned} \tag{4-6}$$

Although the model is clearly oversimplified it accounts for the major features of our results. For comparison, the dashed and solid lines in Figure 4-7 also show the results of the basic Fuchs-Sondheimer model (Equation 4-2) and the model with an insulating layer of thickness t_0 (Equations 4-5, 4-6).

Several conclusions can be drawn from these results. First, the value of σ_0 is close to that of pure Cu at the deposition temperature, $54 (\mu\Omega \text{ m})^{-1}$, and the data are consistent with this value being uniform for $t > 8$ nm. Above this thickness, then, the film consists of reasonably pure Cu (see below). Second, the value of $\tilde{\ell}$ indicates a high level of diffuse scattering. In fact, if Equation 4-3 is taken literally we find that the average specular parameter $p_{ave} = (p_v + p_s)/2$ is very small or even negative: $-0.37 < p_{ave} < 0.11$. Negative p values, while apparently unphysical, have been observed previously [30,33] and indicate a breakdown in the approximations of the Fuchs-Sondheimer theory, notably the assumption of plane parallel surfaces. The AFM images shown here clearly show the inadequacy of this assumption. Nevertheless if surface scattering is dominant the low value of $\tilde{\ell}$ shows that the Cu conduction electrons see very rough boundaries at *both* interfaces. The roughness of the Si/Cu interface may arise from the interdiffusion of Cu and Si as suggested by Demczyk *et al.* [14]

The low value of $\tilde{\ell}$ could also, however, indicate a high level of internal grain-boundary scattering rather than, or in addition to, scattering from rough interfaces. Scattering from internal defects is normally assumed to be independent of thickness, but in thin film growth the grain size often increases with t , as our AFM images suggest. In that case grain-boundary scattering can give a thickness-dependent resistivity that closely approximates Equation (4-2) [28,29,34]. Our data cannot distinguish between these mechanisms.

4-4. Conclusions

Cu films grown on H-terminated Si(100) represent an unusual and useful system. Epitaxial growth occurs readily with little sensitivity to background pressure, deposition rate or substrate temperature, and in spite of a 6% lattice mismatch and a rough and atomically mixed interface. These remarkable features are worthy of study in their own right, and also give the films great utility as a seed layer, [1-9] a model system for training students, [19] and a substrate for surface studies. We have determined the films' surface morphology, which is smooth on the nm scale though not on the atomic scale (RMS roughness 1-2 nm) and by quantifying the effects of deposition rate, substrate temperature and post-deposition annealing — the smoothest films are obtained near room temperature, without annealing, at deposition rates below 3 nm/s.

For thicknesses below 5-10 nm the films consist of disconnected grains, but those grains are structurally indistinguishable from pure Cu. There is no silicide formation. The high level of surface scattering observed in electrical measurements, however, suggests

that the Cu-Si interface, as well as the Cu-vacuum interface, is quite rough on the atomic scale. It remains a puzzle how such excellent and robust epitaxy is achieved in a system that departs so radically from the ideal of layer-by-layer growth. More detailed studies of film structure and composition during the initial stages of growth may help to resolve the issue.

References

- [1] E. T. Krastev, L. D. Voice, and R. G. Tobin, *J. Appl. Phys.* **79** (9), 6865 (1996).
- [2] C.-A. Chang, *Surf. Sci.* **237**, L421-L423 (1990).
- [3] C.-A. Chang, *J. Appl. Phys.* **68**, 5893 (1990).
- [4] C.-A. Chang, *J. Vac. Sci. Technol. A* **8**, 3779 (1990).
- [5] C.-A. Chang, *J. Vac. Sci. Technol. A* **9**, 98 (1991).
- [6] Y.-T. Cheng, Y.-L. Chen, M.M. Karmarkar and W.-J. Meng, *Appl. Phys. Lett.* **59**, 953 (1991).
- [7] Y.-L. Chen and Y.-T. Cheng, *Mat. Lett.* **15**, 192 (1992).
- [8] Y.-T. Cheng and Y.-L. Chen, *Appl. Phys. Lett.* **60**, 1951 (1992).
- [9] R. Naik, M. Ahmad, G.L. Duifer, C. Kota, A. Poli, Ke Fang, U. Rao and J.S. Payson, *J. Magnetism and Magnetic Mat.* **121**, 60 (1993).
- [10] T. Ohmi, T. Saito, T. Shibata, and T. Nitta, *Appl. Phys. Lett.* **52**, 2236 (1988).
- [11] M. Sonowski, H. Usui and I. Yamada, *J. Vac. Sci. Technol. A* **8**, 1470 (1990).
- [12] C.-A. Chang, *J. Appl. Phys.* **67**, 566 (1990).
- [13] C.-A. Chang, J.C. Liu, and J. Angilello, *Appl. Phys. Lett.* **57**, 2239 (1990).
- [14] B.G. Demczyk, R. Naik, G. Auner, C. Kota and U. Rao, *J. Appl. Phys.* **75**, 1956 (1994).
- [15] T. Takahagi, I. Nagai, I. Ishiyani, H. Kuroda and Y. Nagasawa, *J. Appl. Phys.* **64**, 3516 (1988).
- [16] T. Takahagi, I. Ishiyani, H. Kuroda, Y. Nagasawa, H. Ito and S. Wakao, *J. Appl. Phys.* **68**, 2187 (1990).
- [17] Y.J. Chabal, G.S. Higashi, K. Raghavachari and V.A. Burrows, *J. Vac. Sci. Technol. A* **7**, 2104 (1989).

- [18] P. Dumas, Y.J. Chabal and G.S. Higashi, *Phys. Rev. Lett.* **65**, 1124 (1990).
- [19] Minsu Longiaru, E. T. Krastev, and R. G. Tobin, *J. Vac. Sci. Technol., A*, **14**(5), (1996).
- [20] J. Yang, C. Wang, K. Tao and Y. Fan, *J. Vac. Sci. Technol. A* **13**, 481 (1995).
- [21] J.S. Kallend, U.F. Kocks, A.D. Rollett, H.-R. Wenk, *Materials Science and Engineering, A* **132**, 1 (1992).
- [22] H.-R. Wenk, *Preferred Orientation in Deformed Metals and Rocks: An Introduction to Modern Texture Analysis*, (Academic Press, New York, 1985).
- [23] Digital Instruments Nanoscope III Scanning Probe Microscope.
- [24] G. Fischer, H. Hoffmann and J. Vancea, *Phys. Rev. B* **22**, 6065 (1980).
- [25] A.A Baski and H. Fuchs, *Surf. Sci.* **313**, 275 (1994).
- [26] K. Fuchs, *Proc. Cambridge Phi. Soc.* **34**, 100 (1938).
- [27] E.H. Sondheimer, *Adv. Phys.* **1**, 1, (1952).
- [28] P. Wissmann, in *Surface Physics*, edited by G. Höhler, Springer Tracts in Modern Physics 77 (Springer, New York, 1975).
- [29] D. Schumacher, *Surface Scattering Experiments with Conduction Electrons*, edited by G. Höhler, Springer Tracts in Modern Physics 128 (Springer, New York, 1993).
- [30] H. Sugawara, T. Nagano and A. Kinbara, *Thin Solid Films* **21**, 33 (1974).
- [31] H. Sugawara, T. Nagano, K. Uozumi and A. Kinbara, *Thin Solid Films* **14**, 349 (1972).
- [32] J. Bass, in *Landolt Börnstein Numerical Data and Functional Relationships in Science and Technology*, vol. 15, edited by K.-H. Hellwege (Springer-Verlag, Berlin, 1982)
- [33] D. Dayal and P. Wissmann, *Thin Solid Films* **44**, 185 (1977), and references therein.
- [34] A.F. Mayadas and M. Shatzkes, *Phys. Rev. B* **1**, 1382 (1970).
- [35] L.J. van der Pauw, *Phillips Research Reports* **13**, 1 (1958).

Chapter 5

Multiple mechanisms for adsorbate-induced resistivity: Oxygen and formate on Cu(100)

5-1. Introduction

In Chapter 4 I discussed the techniques of growing of epitaxial Cu(100) thin films on Si(100) substrates in high vacuum (HV, base pressure 10^{-8} Torr) and their crystal structure, surface morphology and electrical conductivity. In Chapter 3 I presented the equipment we build in order to grow the Cu(100) films in ultra-high vacuum (UHV; base pressure $< 2 \times 10^{-10}$ Torr). This chapter is dedicated to simultaneous *in situ* adsorbate-induced reflectance and resistivity change measurements of our thin copper films, performed in UHV.

Recent years have seen a resurgence of interest in adsorbate-induced changes in the electrical transport properties of metals. It has been known for many years that adsorbates change (usually increase) the resistance of thin metal films [1-6]. Models proposed to explain these changes include modification of the conduction electron density in the near-surface region caused by direct charge transfer to (or from) the adsorbed molecules [7,8]; a reduction in the effective thickness of the film [9], and the scattering of conduction electrons by the localized potential of the adsorbate [1,3,10,11]. The scattering model has generally been the most successful and widely accepted.

With the development of high-quality surface infrared spectroscopy, adsorbate-induced decreases in the broadband reflectance (*i.e.* far from any vibrational resonance) of bulk metal crystals have been measured [12-24]. The changes are too large and of the wrong sign to be explained by the dielectric properties of the adsorbed layer itself [25], so they are attributed to changes in the substrate's electronic properties. Early results on W and Mo were attributed to a surface electronic state [15] and such a state has also been invoked as a partial explanation for H on Cu(111) [19]. A series of careful spectroscopic experiments on Cu [16-22] and Pt [24] single crystals have strongly supported the scattering model. Theoretical work by Persson and Volokitin has extended the model to explain resistivity changes, reflectance changes, and antiabsorption resonances due to hindered rotations and translations of the adsorbates [18,19,26-30].

The scattering model predicts that the fractional reflectance change $\Delta R/R$ of a bulk sample, for *p*-polarized light at near-grazing incidence, is proportional to the dc resistivity change $\Delta\rho$ of a thin film of the same material under the same surface conditions [20,26]:

$$\frac{\Delta R}{R} = -\left(\frac{4ne^2}{mc \cos\theta}\right)(t\Delta\rho) . \quad (5-1)$$

Here t is the film thickness, n is the electron density, assumed to be unaffected by the adsorbates; m is the effective mass, and θ is the angle of incidence of the light. The frequency must be sufficiently high, $\omega \gg 1/\tau$, v_F/δ , where τ is the bulk electron scattering time, v_F is the Fermi velocity and δ is the classical skin depth. The quantity $t\Delta\rho$ is independent of film thickness [1,3]. The proportionality between $\Delta R/R$ and $t\Delta\rho$ is quite general. It requires the Drude approximation for the metal's dielectric function, that the

adsorbates affect only τ and not n , and a slab model for the depth dependence of the conductivity [20]. Most modifications of the model, such as relaxing the slab model, using separate scattering times for dc and optical frequencies, incorporating film anisotropy, etc., will affect the value of the proportionality constant, but not the structure of Eq. 5-1, in which $\Delta R/R$ and $t\Delta\rho$ are related through a constant *that depends only on the substrate, not on the adsorbate*.

There have been only a few attempts to test Eq. 5-1. Lin *et al.* compared reflectance measurements on bulk single crystals with published resistivity data for polycrystalline films, and found rough agreement for CO and O on Cu, but a large discrepancy for CO on Ni [20]. Because the reflectance and resistance measurements were made on different samples under different conditions, the comparison was unavoidably rough. Hein and Schumacher made simultaneous near-IR reflectance and resistance measurements for oxygen, CO and Cu on Cu films and for Ag on a Ag film [31]. They confirmed the proportionality predicted by Eq. 5-1, but their coefficients were larger than predicted by factors of 1.2 - 3.5 and varied considerably from sample to sample. Their films were deposited by thermal evaporation onto glass slides, giving polycrystalline films with probably a predominant (111) texture [3].

We present the results of simultaneous measurements of the changes in dc resistivity and nonresonant infrared reflectance induced by oxygen and formate adsorption on epitaxial Cu(100) thin films. For oxygen we confirm the linear relationship predicted by the scattering model. Formate adsorption on identically prepared samples, however, caused *no measurable reflectance change*, despite a resistivity change comparable to that

induced by oxygen. This surprising behavior strongly contradicts the scattering model. It implies, first, that formate is a very weak scatterer and, second, that formate induces a resistivity change through a different mechanism, probably a reduction in conduction electron density.

5-2. Experimental

The samples were epitaxial Cu(100) films grown *in situ* in ultrahigh vacuum on Si(100) substrates. Contact strips (150 nm Ag on 10 nm Cr) were deposited on 1 × 2 cm pieces of Si in a separate evaporator. The samples were then etched in a 10% aqueous HF solution as described elsewhere [32,33], removing the native oxide and leaving a hydrogen-passivated surface. The sample was mounted on a custom-designed sample holder that incorporates four electrical contacts for the resistivity measurements and two thermocouple contacts and provides a temperature range of 100 to 900 K [34] and immediately (within a few minutes) transferred into UHV via a high-vacuum load-lock. The sample was baked in UHV at 725 K for 15 minutes to remove impurities before deposition of the Cu.

The Cu films were grown by resistive thermal evaporation. A liquid-nitrogen-cooled shield maintained the pressure during deposition in the range of 5 - 10 × 10⁻¹⁰ Torr. The sample temperature was 300 - 310 K, the deposition rate was 0.1 - 0.5 nm/s and the film thickness was typically 50 nm, measured with a quartz-crystal thickness monitor calibrated against a diamond-stylus profilometer. We have shown that films grown in this way in HV are fully epitaxial, but have rms surface roughness of 1-2 nm [32]. X-ray diffraction and AFM studies of the UHV-grown films showed that they are epitaxial and

with a comparable surface roughness to the HV-grown films. The films exhibited hazy low energy electron diffraction spots characteristic of their (100) orientation, confirming epitaxy and indicating surface ordering on a length scale ~ 10 nm. Auger electron spectroscopy detected carbon and oxygen at levels of less than 5 atomic percent, with no other impurities above $\sim 2\%$. The samples had room temperature resistivities of 3 - 6 $\mu\Omega$ cm, two to four times higher than pure Cu, independent of film thickness (for $t > 50$ nm). Copper films of comparable thickness (50 nm) grown in high-vacuum conditions show room temperature resistivity of 3 $\mu\Omega$ cm (see Figure 4-7) and at higher thickness their resistivity approaches the value for the pure copper (1.7 $\mu\Omega$ cm). Currently we are investigating the reason(s) for the higher resistivity of the UHV-grown films.

The infrared spectroscopic system has been described elsewhere [24]; it permits measurements of nonresonant reflectance changes at a fixed frequency (350 - 3000 cm^{-1}) with a sensitivity of 0.02%. All measurements reported here were made at a frequency of 2650 cm^{-1} , well away from any vibrational resonances and in a frequency range where the approximations appropriate to Eq. 5-1 are well satisfied [21]. The film resistance was measured by a quasi-four-wire ac lock-in technique (sensitive to contact resistance but not to lead resistances), using a 1.0 mA current modulated at 3 kHz. Fractional resistance changes $\Delta V/V < 10^{-4}$ were easily measurable.

All measurements were made at room temperature. Gas exposures were accomplished by backfilling the chamber and were calculated from the uncorrected pressure measured at the ionization gauge. The formic acid was purified by repeated freeze-pump-thaw cycles. Formic acid is known to dissociate on Cu, leaving adsorbed

formate (HCOO) and hydrogen [22,35,36]. At room temperature we expect the hydrogen to leave the surface. Auger spectroscopy after formic acid dosing revealed increased C and O signals consistent with formate adsorption.

5-3. Results and Discussion

A typical combined resistivity and reflectance measurement for oxygen on Cu(100) is shown in Figure 5-1. Figure 5-1a shows the fractional reflectance change of a Cu(100) film (thickness 49 nm) as a function of time. Figure 5-1b shows the fractional resistivity change. A linear baseline has been subtracted from both curves. At 100 s, 5×10^{-7} Torr O_2 was introduced into the chamber for 100 s. The reflected IR intensity decreased sharply, accompanied by a sharp increase in the resistivity. The maximum fractional reflectance change $\Delta R/R$ was -0.0070 ± 0.0005 and the maximum fractional resistivity change $\Delta \rho/\rho$ was 0.032. When the oxygen was turned off, the reflectance increased (and resistance decreased) slightly, probably due to oxygen leaving the surface.

In the period before and after dosing, the rms fluctuation in $\Delta R/R$ is 0.0004; this represents the uncertainty in each point. Since we have 40-50 independent measurements both before and after the dose, the statistical uncertainty in the overall reflectance change is reduced to 0.0001. The uncertainty in $\Delta R/R$, however, is generally dominated by systematic uncertainty in the baseline subtraction.

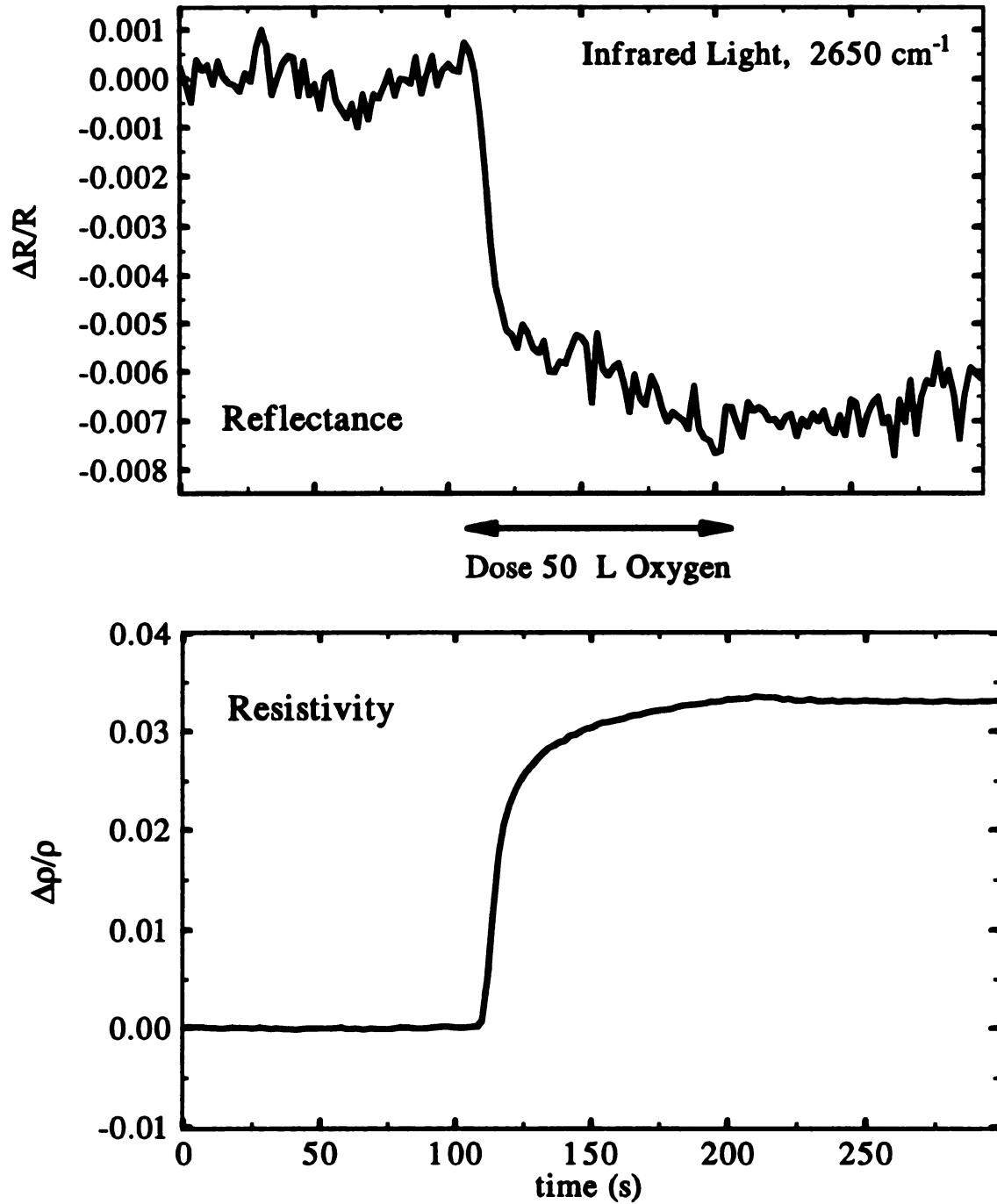


Figure 5-1. a) Fractional reflectance change at 2650 cm^{-1} for oxygen on epitaxial Cu(100). The film was 49 nm thick. At 110 s the sample was exposed to 5×10^{-7} Torr O_2 for 100 s. b) Fractional dc resistivity change measured simultaneously with (a).

Figure 5-2 shows a plot of $\Delta R/R$ vs. $t\Delta\rho$ for the dosing period, from Figure 5-1.

The error bar, which is the same for all the points, represents the single-point rms noise of ± 0.0004 . Although neither the resistivity nor the reflectance varies linearly with exposure, the relationship between them is linear, as predicted by the scattering model (Eq. 5-1).

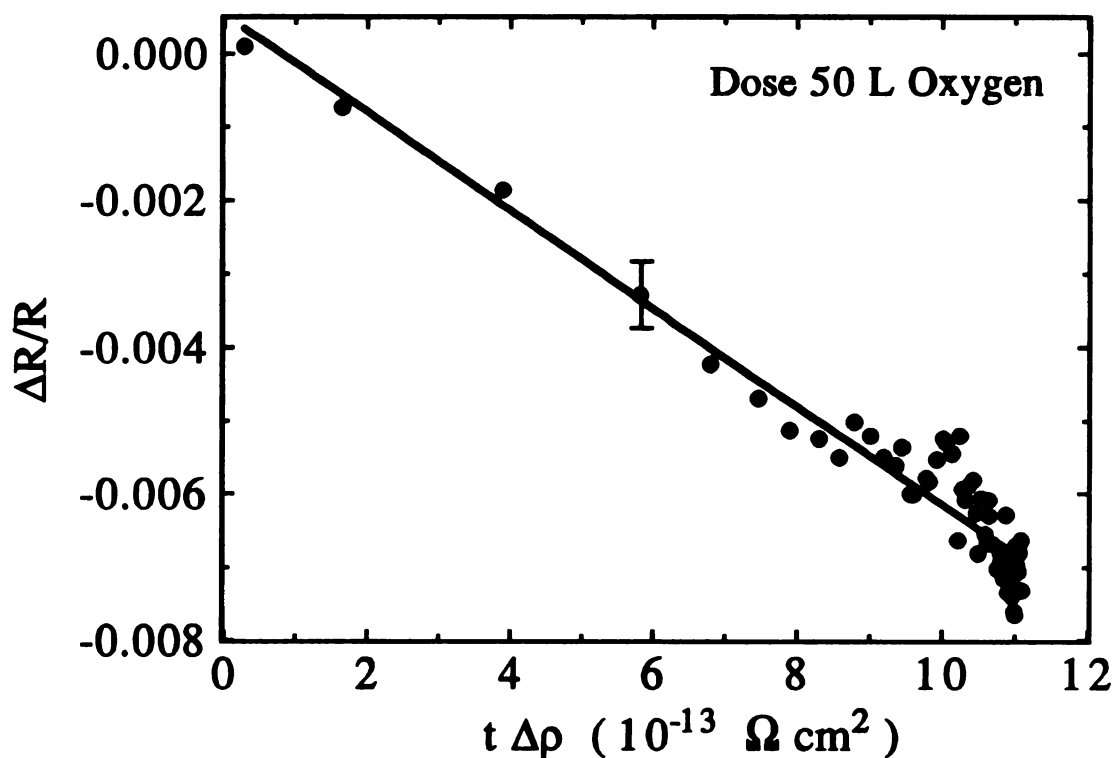


Figure 5-2. Fractional reflectance change $\Delta R/R$ vs. $t\Delta\rho$ for oxygen on epitaxial Cu(100), from Fig. 1. The error bar shown is typical of all the points.

The value of ne^2/mc deduced from the slope is $1.2 \times 10^8 \Omega^{-1} \text{ cm}^{-2}$. The failure of the line to pass through the origin is attributable to a small discrepancy in the time scales of the two measurements; it does not affect the value of the slope. We performed five similar

experiments on different samples, always obtaining a linear relationship between $\Delta R/R$ and $t\Delta\rho$, with values of ne^2/mc varying from 0.6 to $1.2 \times 10^8 \Omega^{-1} \text{cm}^{-2}$. Table 5-1 compares our value of ne^2/mc for oxygen on Cu with the data of Hein and Schumacher [31]. The experimental values show a wide spread and in most cases deviate from the theoretical

Table 5-1. Values of the coefficient ne^2/mc deduced from the slope of $\Delta R/R$ vs. $t\Delta\rho$.

	ne^2/mc [$10^9 \Omega^{-1} \text{cm}^{-2}$]	Source
Theoretical for pure Cu	0.61	
O/Cu(100)	0.06 - 0.12	This work
O/poly Cu	2.13	Ref. 31
CO/poly Cu	1.06	Ref. 31
Cu/poly Cu	0.71	Ref. 31
Formate/Cu(100)	< 0.01	This work

value based on the electron density in bulk copper. We return to these numerical discrepancies below; at this point we emphasize that the linear relationship predicted by the scattering model is well confirmed for oxygen on Cu.

A more stringent test of the scattering model can be made by comparing different adsorbates on identically prepared substrates. Figure 5-3 presents a combined resistivity-reflectance measurement for formic acid dosing on a Cu(100) thin film (thickness 51 nm) grown under conditions identical to those used for Figure 5-1. The resistances of the two

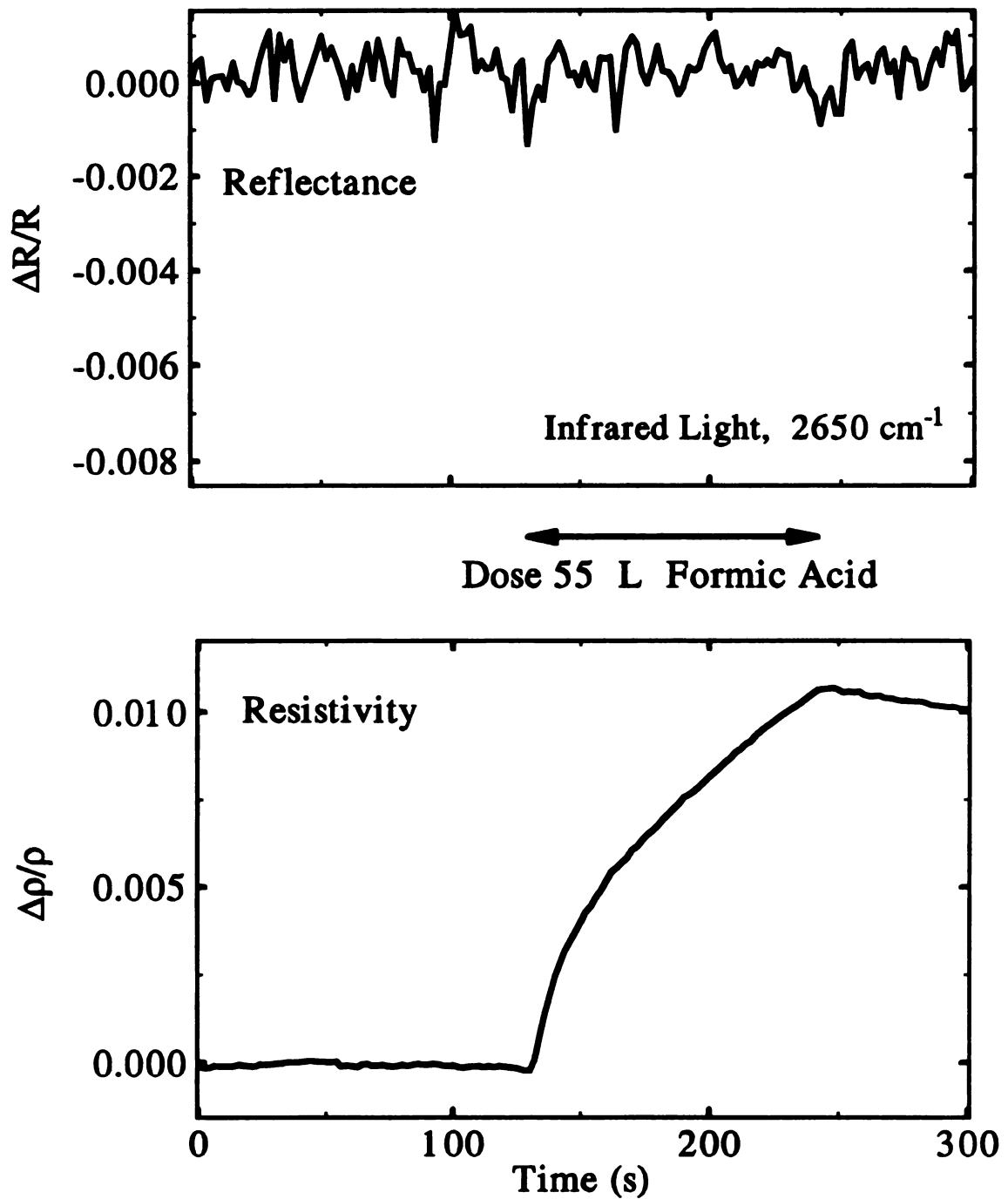


Figure 5-3. a) Fractional reflectance change at 2650 cm^{-1} for formate on epitaxial Cu(100). The film was 51 nm thick. At 130 s the sample was exposed to 5×10^{-7} Torr formic acid for 110 s. No reflectance change is observable. b) Fractional dc resistivity change measured simultaneously with (a).

films differed by only 15%. Similar results were obtained in three other experiments on different samples. The formic acid dose was 5×10^{-7} Torr for 110 s. The maximum $\Delta\rho/\rho$ was 0.011. In sharp contrast to the oxygen case, however, *no reflectance change is detectable*. Based on the noise level and baseline stability, we can set an upper limit of 0.0002 on $\Delta R/R$, leading to a nominal value of ne^2/mc less than $0.1 \times 10^8 \Omega^{-1} \text{ cm}^{-2}$, at least a factor of ten smaller than for oxygen on an identically prepared sample.

This striking deviation from the scattering model demonstrates, first, that the scattering cross section for formate is anomalously small, and second, that another process must be responsible for the resistance change. Assuming a formate coverage of 0.5 monolayer (ML: 1 ML represents one formate per surface copper atom), we set an upper limit on the scattering cross section for formate of 0.04 \AA^2 , as compared with 0.8 \AA^2 for CO on Pt(111), itself a weak scatterer [24]. The lack of a reflectance change for formate on Cu(100) was previously reported by Lin *et al.* [21,22] from single crystal experiments, and tentatively explained in terms of the absence of an adsorbate-derived electronic state close to the Fermi level [22].

The resistance change for formate is most readily explained by a change in the conduction electron density n . Within a Drude model, which is a good approximation for Cu at infrared frequencies [37], the resistivity and reflectance changes of a film of thickness t are given to first order by [15,20]:

$$\begin{aligned} \frac{\Delta\rho}{\rho} &= -\frac{\ell_B}{t} \left[\frac{\Delta n}{n} + \frac{\Delta\tau}{\tau} \right] \\ \frac{\Delta R}{R} &= \frac{4\ell_B}{c\tau \cos\theta} \frac{\Delta\tau}{\tau} \end{aligned} \tag{5-2}$$

where the changes in n and τ are assumed to affect a slab of thickness $\ell_B = v_F\tau$, the bulk electron mean free path, and t is larger than the skin depth. (Eq. 5-1 is recovered if $\Delta n = 0$.) A change in n will affect the resistivity but not the reflectance, as we observe for formate [38]. If we assume a bulk electron density n equal to that of pure Cu and a maximum formate coverage of 0.5 ML, the observed resistivity changes require that each formate molecule bind approximately nine conduction electrons — an implausibly large number.

We suggest, however, that n in our films is considerably smaller than in pure Cu. If the high room temperature resistivity of our films compared to pure Cu (see section 2) is due to n , then each formate would need to bind only 2-3 electrons to account for our results, a far more plausible number. A reduced value of n would also partially explain the low values of ne^2/mc deduced from our reflectance vs. resistance curves (Table 5-1). We observe a weak but positive correlation between ne^2/mc and the film conductivity, which tends to support this hypothesis. Reduced n (by as much as a factor of 50) has been observed previously in films of Cu and other metals and explained by localization of electrons within microcrystallites or at grain boundaries [11,39-41].

In summary, we have found that the mechanism for adsorbate-induced resistance changes is chemically specific. While the scattering model successfully explains results for a number of systems, including oxygen on Cu(100), it fails in the case of formate on Cu(100). On identically prepared films, the ratio of the reflectance change to the resistivity change is at least a factor of ten smaller for formate than for oxygen. It is likely that the resistance increase induced by formate is caused by a reduction in the conduction

electron density. Chapter 5 is based on our paper, published in *Surface Science Letters*

[42].

References

- [1] P. Wissmann in *Surface Physics*, ed. G. Höhler, Springer Tracts in Modern Physics Vol. 77 (Springer, New York, 1975).
- [2] D. Dayal, H.-U. Finzel and P. Wissmann in *Thin metal films and gas chemisorption*, edited by P. Wissmann (Elsevier, Amsterdam, 1987).
- [3] D. Schumacher, *Surface Scattering Experiments with Conduction Electrons*, edited by G. Höhler, Springer Tracts in Modern Physics Vol. 128 (Springer, New York, 1993).
- [4] T.J. Coutts, *Electrical Conduction in Thin Metal Films* (Elsevier, Amsterdam, 1974).
- [5] M.R. Shanabarger, *J. Vac. Sci. Technol. A* **4**, 623 (1986).
- [6] A.F. Hebard, R.R. Ruel and C.B. Eom, *Phys. Rev. B* **54**, 14 052 (1996).
- [7] R. Suhrmann and K. Schulz, *Z. Phys. Chem. (Frankfurt)* **1**, 69 (1954).
- [8] G. Wedler and M. Fouad, *Z. Phys. Chemie Neue Folge*, **40**, 12 (1964).
- [9] W.M.H. Sachtler and G.J. H. Dorgelo, *Z. Phys. Chem. (Frankfurt)* **25**, 69 (1960).
- [10] K. Fuchs, *Proc. Cambridge Phil Soc.* **34**, 100 (1938).
- [11] E.H Sondheimer, *Adv. Phys.* **1**, 1 (1952).
- [12] D.M. Riffe, L.M Hanssen and A.J. Sievers, *Phys. Rev. B* **34**, 692 (1986).
- [13] D.M. Riffe, L.M Hanssen and A.J. Sievers, *Surf. Sci.* **176**, 679 (1986).
- [14] V.A. Burrows, S. Sundaresan, Y.J. Chabal and S.B. Christman, *Surf. Sci.* **180**, 110 (1987).
- [15] J.E. Reutt, Y.J. Chabal and S.B. Christman, *Phys. Rev. B* **38**, 3112 (1988).
- [16] C.J. Hirschmugl, G.P. Williams, F.M. Hoffmann and Y.J. Chabal, *Phys. Rev. Lett.* **65**, 480 (1990).
- [17] C.J. Hirschmugl, Y.J. Chabal, F.M. Hoffmann and G.P. Williams, *J. Vac. Sci. Technol. A* **12**, 2229 (1994).

- [18] C.J. Hirschmugl, G.P. Williams, B.N.J. Persson and A.I. Volokitin, *Surf. Sci.* **317**, L1141 (1994).
- [19] C.L.A. Lamont, B.N.J. Persson and G.P. Williams, *Chem. Phys. Lett.* **243**, 429 (1995).
- [20] K.C. Lin, R.G. Tobin, P. Dumas, C.J. Hirschmugl and G.P. Williams, *Phys. Rev. B* **48**, 2791 (1993).
- [21] K.C. Lin, R.G. Tobin and P. Dumas, *Phys. Rev. B* **49** (1994) 17 273; *ibid.* **50**, 17 760 (1994).
- [22] K.C. Lin, R.G. Tobin and P. Dumas, *J. Vac. Sci. Technol. A* **13**, 1579 (1995).
- [23] J. Dvorak, E. Borguet and H.-L. Dai, *Surf. Sci.* **369**, L122 (1996).
- [24] D.E. Kuhl, K.C. Lin, C. Chung, J.S. Luo, H. Wang and R.G. Tobin, *Chem. Phys.* **205**, 1 (1996).
- [25] R.G. Tobin, *Phys. Rev. B* **45**, 12 110 (1992).
- [26] B.N.J. Persson, *Phys. Rev. B* **44**, 3277 (1991).
- [27] B.N.J. Persson, *Chem. Phys. Lett.* **197**, 7 (1992).
- [28] B.N.J. Persson and A.I. Volokitin, *Surf. Sci.* **310**, 314 (1994).
- [29] A.I. Volokitin and B.N.J. Persson, *Phys. Rev. B* **52**, 2899 (1995).
- [30] P. Dumas, M. Suhren, Y.J. Chabal, C.J. Hirschmugl and G.P. Williams, *Surf. Sci.* **371**, 200 (1997).
- [31] M. Hein and D. Schumacher, *J. Phys. D* **28**, 1937 (1995). Their Eq. 6 differs from my Eq. 5-1 because of their use of unpolarized light and a smaller angle of incidence. We have used their Eq. 6 in analyzing their data.
- [32] E.T. Krastev, L.D. Voice and R.G. Tobin, *J. Appl. Phys.* **79**, 6865 (1996).
- [33] M. Longiaru, E.T. Krastev and R.G. Tobin, *J. Vac. Sci. Technol. A* **14**, 2875 (1996).
- [34] E.T. Krastev and R.G. Tobin, submitted to *J. Vac. Sci. Technol.*
- [35] B.A. Sexton, *Surf. Sci.* **88**, 319 (1979).

[36] P.A. Taylor, P.B. Rasmussen, C.V. Ovessen, P. Stoltze and I. Chorkendorff, Surf. Sci. **261**, 191 (1992).

[37] M.A. Ordal, R.J. Bell, R.W. Alexander, Jr., L.L Long and M.R. Querry, Appl. Opt. **24**, 4493 (1985).

[38] We are assuming that τ remains constant; this differs slightly from the assumption of constant ℓ_B considered in Refs. 1,6-8.

[39] H. Hoffmann and J. Vancea, Thin Solid Films **85**, 147 (1981).

[40] J. Vancea and H. Hoffmann, Thin Solid Films **92**, 219 (1982).

[41] J. Vancea, H. Hoffmann and K. Kastner, Thin Solid Films **121**, 201 (1984).

[42] E. T. Krastev, D. E. Kuhl and R. G. Tobin, Surf. Sci. Lett., **387**, L1051, (1997)

Chapter 6

Conclusion

The way adsorbed molecules affect the electron dynamics in the near surface region of metals has been actively investigated both experimentally and theoretically during the last years. A theory which correlates the presence of alien molecules on the clean metal surface with an increased diffuse scattering of the conduction electrons [1-4] has been established as dominant. The theory predicts a linear relationship between reflectance change $\Delta R/R$ and resistivity change $\Delta\rho$, with a proportionality constant that does *not* depend on the type of adsorbate. The research presented in this dissertation was concentrated on testing the above model by experimental examining the relationship between $\Delta R/R$ and $\Delta\rho$.

My work comprised the following three stages:

1. Design of UHV sample transfer, sample handling and thin film evaporation equipment. The developed system was optimized for infrared reflectance and resistivity measurements and incorporates several features that are not commercially available -- grazing optical access and transfer of large samples with six breakable electrical contacts.

2. Development of methods for growing epitaxial Cu(100) thin films on H-terminated silicon substrates. Thorough characterization of their crystal structure, surface morphology and electronic properties. Despite the large lattice mismatch between copper and silicon, etching of the substrates in aqueous solution of hydrofluoric acid (HF) allows growing of highly epitaxial films by simple thermal evaporation and with minimal *in situ* preparation. Although epitaxial, the films are microscopically rough, showing RMS surface roughness of 1-2 nm on a $1\mu m^2$ scale.

3. Investigation of the changes in the resistivity and the broadband reflectance of the films caused by adsorbates. Simultaneous *in situ* resistivity-reflectance measurements were performed using oxygen and formate as adsorbates and the results were analyzed from the point of view of the scattering theory.

Although the heart of my study is the resistivity-reflectance change experiments, all three stages should be considered as a whole as the first two were crucial for performing accurate measurements and obtaining reliable and respectable results. Most of my work was presented in four articles, published in reputable scientific journals [5-8].

For the case of oxygen adsorption the linearity between $\Delta R/R$ and $\Delta\rho$ was observed in agreement with the scattering mechanism. However a discrepancy was found between the experimental and theoretical values of the proportionality constant. The lower value found in our experiments could be attributed in part to a lower, compared to bulk, concentration of conducting electrons in our films. Lower conduction electron

concentration has been experimentally observed before [9,10] and is consistent with the fact that our films have higher resistivity than single crystal copper.

For the case of formate adsorption on *identically* prepared films a considerable resistivity change was found with *no* measurable reflectance change. This result is in striking contradiction with the statement of the scattering theory, that the relationship between $\Delta R/R$ and $\Delta\rho$ is adsorbate independent. Therefore it can be concluded that the mechanism of the adsorbate induced resistivity change is chemically specific and a mechanism other than scattering must be responsible for the resistivity change observed for formate. One possible reason could be a decrease in the conduction electron density due to binding of electrons by the formate species on the surface.

Obviously there is an imminent need for more experimental work exploring other adsorbate - thin film systems. A good potential candidate is the system O/Ni(100), which could also show a deviation from the scattering model, as suggested by a previous study [14]. The investigation of the above system would be facilitated by the fact that epitaxial Ni(100) films can be easily grown on silicon, using copper as a seed layer [20].

The scientific significance of my work can be seen in the following aspects:

1. This is the first study experimentally probing the relationship between the adsorbate induced resistivity and reflectance change, performed *in situ* and on well characterized *epitaxial* films.

2. My work rigorously demonstrates a *deviation* from the scattering mechanism. Previous studies performed on single crystals [11-18] and thin films [19] generally show support to the scattering theory to greater or lesser extent. This work indicates that other mechanisms or a combination of several should also be considered while trying to clarify the effects of adsorbates on the electron dynamics in the close vicinity of the metal surface.

3. My research has been directly involved with the issue of energy transfer between moving adsorbates and substrate degrees of freedom, which is of large importance in the fast developing field of nanoscale tribology -- the study of atomic scale friction. It also rises several intriguing questions for the surface scientist. What are the mechanisms underling the formate induced resistivity change? Is the relation between resistivity and reflectance change adsorbate independent even for systems where the scattering mechanism is dominant and the linearity holds?

4. If the resistivity and reflectance changes are not so simply related by adsorbate independent constant, the combination of the two measurements could provide a measure of *chemical selectivity* in potential gas sensing methods.

Based on the above I consider my study as a strong motivation for further experimental and theoretical investigation aimed at better understanding of the complicated phenomena occurring at the gas-metal interface and their possible implementation in gas sensing applications. Apart from studying other adsorbate -

substrate systems, further experimental work concerning coverage, temperature and frequency dependence of the adsorbate induced resistivity-reflectance change would be strongly beneficial. From a theoretical point of view further development is needed in order to explain the formate/Cu(100) behavior and build a more integral picture of the acting mechanisms, through which different adsorbates affect the electron dynamics in the near-surface region of metals.

References

- [1] B.N.J. Persson, *Phys. Rev. B* **44**, 3277 (1991).
- [2] B.N.J. Persson, *Chem. Phys. Letters* **185**, 292 (1991) .
- [3] B.N.J. Persson, *Chem. Phys. Letters* **197**, 7 (1992).
- [4] B.N.J. Persson and A.I. Volokitin, *Surface Sci.* **310**, 314 (1994).
- [5] E. T. Krastev, L. D. Voice, and R. G. Tobin, *J. Appl. Phys.* **79** (9), 6865 (1996).
- [6] Minsu Longiaru, E. T. Krastev, and R. G. Tobin, *J. Vac. Sci. Technol. A*, **14**(5), 2875 (1996).
- [7] E. T. Krastev, D. E. Kuhl and R. G. Tobin, "Multiple mechanisms for adsorbate-induced resistivity - Oxygen and Formate on Cu(100)", in press *Surf. Sci. Lett.*
- [8] E. T. Krastev and R. G. Tobin, "Ultrahigh vacuum sample transfer system with multiple electrical connections and grazing optical access", submitted to *J. Vac. Sci. Technol.*
- [9] J. Vancea, H. Hoffmann, *Thin Solid Films*, **92**, 219 (1982).
- [10] J. Vancea, H. Hoffmann, K. Kastner, *Thin Solid Films*, **121**, 201 (1984).
- [11] C.J. Hirschmugl, G.P. Williams, F.M. Hoffmann and Y.J. Chabal, *Phys. Rev. Letters* **65**, 480 (1990).
- [12] C.J. Hirschmugl, Y.J. Chabal, F.M. Hoffmann and G.P. Williams, *J. Vac. Sci. Technol. A* **12**, 2229 (1994).
- [13] C.J. Hirschmugl, G.P. Williams, B.N.J. Persson and A.I. Volokitin, *Surface Sci.* **317**, L1141 (1994).
- [14] K.C. Lin, R.G. Tobin, P. Dumas, C.J. Hirschmugl and G.P. Williams, *Phys. Rev. B* **48**, 2791 (1993).
- [15] K.C. Lin, R.G. Tobin and P. Dumas, *Phys. Rev. B* **49** (1994) 17273 (1994); **50**, 17760 (1994).

- [16] B.A Sexton, Surf. Sci. 88, 319 (1979); P.A. Taylor, P.B. Rasmussen, C.V. Ovesen, P. Stoltze, and I. Chorkendorff, Surf. Sci. 261, 191 (1992).
- [17] D.E. Kuhl, K.C. Lin, Chilhee Chung, J.S. Luo, Hong Wang and R.G. Tobin, Chemical Physics 205,1 (1996).
- [18] C.L.A Lamont, B.N.J. Person and G.P. Williams, Chem. Phys. Lett. 243, 429 (1995).
- [19] M. Hein and D. Schumacher, J. Phys. D 28, 1937 (1995).
- [20] Chin-An Chang, J. Vac. Sci. Technol. A 8, 3779 (1990).